

Evaluation on mechanical properties of micro/nano-meter
scale materials by resonant vibration

Fang Hui

Contents

| | |
|---|----|
| Chapter 1: Introduction | 1 |
| Chapter 2: Anisotropic elastic properties of chiral sculptured thin films at micro-scale evaluated by resonance frequency spectra..... | 15 |
| Chapter 3: Size dependence of fatigue damage in sub-micrometer single crystal gold | 37 |
| Chapter 4: Formation of Slip Bands in Nano-polycrystalline Copper under High Cycle Fatigue of SiTiCuSiN Nanoscale Material..... | 59 |
| Chapter 5: Conclusions..... | 81 |

Chapter 1: Introduction

Background

With a recent development and miniaturization of small devices due to the increasing demands for a high-density integration, the component size is approaching micro/nano-meter scale. Industry has intensely developed devices with multifarious function, namely micro-electro-mechanical-system (MEMS) and nano-electro-mechanical-system (NEMS) including small sensors and actuators [1~6]. The devices are composed of numerous micro/nano-scale components which are in the form of films, cantilevers and wires [7].

For engineering purposes, these modules possess mechanical, electrical, and thermal function in the devices. Stress applied to a micro/nano-component stems from various sources such as the mechanical loading, residual stress, and thermal stress in the processing as well as in the service [8]. Some micro components, such as micro radio frequency switches, etc. are constantly subjected to a cyclic load during the period of their service. Hence, they should be carefully designed on the basis of mechanical condition in terms of their reliability, but, there is little known about the design rules and constitutive descriptions of their properties because of experimental difficulty in the scale. It is necessary to study mechanics properties, including elastic and fatigue characteristics of such micro/nano-meter scale components [9]. Especially, it is crucial to develop the experimental methodology for mechanical property of such scale materials. This also brings great progress to get the insight of the fundamental knowledge on the characteristic deformation property and the fatigue mechanism.

Experimental methodology of small components

For several decades, researchers have tried to determine mechanical properties of small specimens experimentally. Measurement of small specimens was demanding, not only because it is difficult to handle them but also because there is a series of new problems caused by the unusually small size. Fixing the micro-scale specimen onto the testing setup was no trivial exercise [10]. It is also difficult to obtain good alignment between the specimen and the set-up. Small imprecision in the setup, which has negligible consequences for usual specimens in macro-scale measurements, can be a major source of systematic measurement error for micro-specimens [11]. Moreover, the deformation of the specimens is very small for micro-components and thus difficult to measure. One of the main efforts in improving the reliability of the micro-specimen testing methods is undertaken by designing advanced loading apparatus and specimens that are less prone to the problems mentioned above [12].

Bending tests are an easier test method to handle a small size specimen than tensile tests. Johansson et al. [13], Weihs et al. [14], Wilson et al. [15], and so on have performed bending tests for Si cantilever beams and have clarified the effect of surface roughness and crystal orientation on the fracture strength of the beams. In order to observe the interface fracture process in a nanometer-scale component in detail, Hirakata et.al [16] have developed a novel method to overcome the experimental difficulties combining a transmission electron microscopy (TEM) and a well-controlled small loading device. A miniature mechanical loading apparatus, which consists of a movable sample stage and a diamond loading tip with a MEMS load sensor, is built in a TEM specimen holder. The alignment resolution of the actuator is approximately 1 nm for the x,

y and z axes. Utilizing this apparatus, Sumigawa et.al [17] got the loading curve of nano-cantilever specimen with the Cu-layer thickness of 20 nm and in-situ TEM images of specimen. Sumigawa et al. [18] observed non-linear behavior of the load-deflection relation which is attributed solely to the plastic deformation of the Cu component since the yield stresses of Si and SiN are much higher than that of Cu. Similar experiments conducted for the same Cu/Si interface with the Cu thickness of 200 nm thick revealed that the crack initiation criterion is independent of the Cu-layer thickness while the plastic property possesses the strong dependence on it [19].

To evaluate the fatigue strength of materials in micrometer scale, the monotonic tension tests have been developed for micro-components. Because the fatigue behavior is sensitive to the stress concentration, one of the main experimental difficulties on the fatigue testing of small material is the loading alignment including specimen gripping [20]. In order to avoid this issue, bending tests have been widely used. Tsuchiya et al developed a testing structure, which is a bridge configuration with a mass in the middle. The fatigue strength of the silicon micro-beam was measured by pushing the mass with an indenter until fracture occurred. By comparing the fracture strength measured with the indenter before and after the oscillation, the authors found the fatigue damage due to the oscillations [21]. However, since the load is applied by tip contact, it is not easy to extend this methodology to the fatigue testing with high-cycle loading in submicron-scale. Moreover, it is difficult to produce reverse loading in such small scale specimen. Thus, in order to characterize the fundamental fatigue property in submicron scale specimen, an advanced test method for high-cycle

fatigue under tension-compression is strongly desired.

Experiments using resonant vibration

The resonance frequency of single freedom system is $f_0 = \frac{1}{2\pi} \sqrt{\frac{Ewt^3}{4d^3m}}$. The dynamics behavior is dependent of Young's modulus and the mass of components. The Young's modulus E and the flexural rigidity are the most fundamental dynamics properties of structures. On the basis of the property, the elastic constants of large materials were evaluated using the resonant frequency [22]. This has potentials for the evaluation of micro/nano-meter materials. A resonance based method has some advantages as compared to previous methods for small materials: (i) a sub - strata for supporting specimen is not needed, (ii) a special actuator for applying force is not necessary, then the misalignment between the specimen and the set-up is not an important issue, (iii) deformation of specimens can be control by the resonance modes, and (iv) the deformation of the specimens is amplified by resonance vibration, and thus easy to measure. In this doctoral dissertation, a new sub-micro vibration method is presented, which can excite and measure the vibration modes of films comprised of helical nano-springs.

Mechanical property of small materials

Small materials have characteristic mechanical properties, which has sometime strong dependence on the size-scale [23]. The size-scale effect on mechanical behaviors can be classified into two categories in terms of structures, (a) internal feature of structure (understructure) and (b) overall physical

dimensions. For a former example (a), it is well known that the yield strengths of metallic alloys can be improved through refinement of the grain size [24, 25, 26], where the yield strength is proportional to the inverse square root of the average grain diameter, and this relation is generally valid for grains that range in size from millimeters to tens of nanometers. For a latter example, the size affect strongly on the mechanical property of film/wire/dot in the nano-meter scale.

There has been reported on the characteristic mechanical properties of solid materials with nano-scale understructures [27]. On the other hand, with technological progress, the complex structure, such as thin films consisting of nanoelements, have the potential to play a key role in novel nano- or micro electromechanical systems (NEMS/MEMS) [28]. Thin films at micro-scale show elastic anisotropy between the in-plane and out-of-plane directions because of discrete structure, residual stress or micro-defects [29], then exhibit transverse isotropy and show several independent elastic constants with a coordinate system. Dynamic oblique deposition (DOD), in which the deposition angle and the in-plane direction of a substrate are changed during deposition, enables us to fabricate a thin film comprised of nanosprings that have helicoid, zigzag, pillar, and other shapes [30]. The method utilizes the atomic self-shadowing effect during physical vapor deposition due to deposition with a highly oblique angle [31]. Spring shape can be precisely controlled by adjusting the incident angle of vapor flux and substrate rotation [32]. These films have layered structures, and the microstructures display an array of myriad pores, interfaces and other defects, with multiple length scales, along with anisotropy and non-linearity in elastic properties [33]. As such, the elastic moduli of the films are a fraction of the

values observed in bulk [34]. Obviously, the theoretic and numerical approaches would not be utilized to evaluate the elastic properties of this complex components in small scale. Most previous experiment studies: flexural vibration of a reed composed of a film–substrate layered plate [35], and nanoindentation [36]. These methods always involve ambiguity caused by the mechanical contacts to grip the specimen and to make the acoustic coupling. Brillium-scattering technique [37] enables a non-contacting measurement, but it is insensitive to non-Rayleigh-wave modes [38]. Determining the anisotropic elastic properties of such films is challenging and remains a subject of scientific and technological interest. From a scientific point of view, they allow extension of experimental techniques and models to complex materials/microstructure, while the derived properties are important for the films with complex micro-structure designs, particularly to address compliance issues. The development of techniques to determine the anisotropic elastic properties enables an understanding of the role of microstructural features and linkages to processing conditions and is also important for design purposes, e.g., sculptured thin films at micro-scale [39].

The development of dynamic techniques to determine the anisotropic elastic properties enables an understanding of the role of micro-structural features and linkages to processing conditions. Dynamics testing methods, such as the ultrasonic method, have also been explored, based on the relationship between ultrasonic wave propagation velocities in a material and its elastic constants. Vibration damping [40, 41], a mechanical spectroscopic method based on non-contact laser vibrometry, has been used to study the damping behavior of

coatings. All the above methodologies determine the weighted value of elastic moduli in a given direction or set of directions.

Some dynamic studies use fixed-free or free-free resonance bar techniques, and composite oscillator techniques [42]. These methodologies determine the weighted value of elastic moduli in a given direction or set of directions. However, singular or averaged values for elastic moduli are inadequate for describing the direction-dependent behavior of anisotropic systems. For measuring elastic constants of anisotropic thin films, researchers have developed a number of methods based on the resonance ultrasound spectroscopy (RUS) technique [43], which can determine independent elastic constants from the mechanical resonance frequencies. But this technique is limited by the geometric characteristics of the specimens, which make it hard to detect the oscillation amplitude from micro-specimens with surfaces measuring tens by tens of micrometers. Little vibration testing has been done on the small anisotropic components due to the difficulties associated with exciting the specimen and detecting oscillation at the micron-scale.

Fatigue property of nanometer scale components

The fatigue behavior is another fundamental mechanical properties of structures. In bulk metals under fully-reversed and high-cycle loading, the extrusion/intrusion, of which stress concentration causes crack initiation, appears on the surface [44]. The extrusion/intrusion is formed along a persistent slip band (PSB), which has an understructure of self-organized dislocations with a thickness of a few micrometers [45]. Since fatigue damage of extrusion/intrusion

has a characteristic width of several micrometers, regardless of the component size in a bulk metal [46], fatigue extrusions would be expected to form in thick metal films with thicknesses of tens of micrometers. It is questionable whether fatigue extrusions/intrusions and typical dislocation structures similar to that observed in bulk materials can form in the thinner films and what the relationship between fatigue damage and the length scale of the tested material is. It is expected that in thinner films with thicknesses of the order of the dimension of dislocation walls in PSBs, the situation is different.

Zhang et.al present experimental observations of fatigue damage and corresponding dislocation structures in thin Cu films as a function of film thickness. In the large grains of the fatigued Cu film 3.0 μm thick, coarse extrusions along slip bands and characteristic dislocation walls, labyrinths and cells, similar to those in fatigued bulk material, were found. When the grain dimensions were smaller than 3.0 μm , because of either film thickness or grain diameter, less extensive finer extrusions were found at the film surface and no characteristic fatigue dislocation structures were observed [47]. For 1.1 μm thick Cu films, Read [48] argued that the absence of clear slip steps on the specimen surfaces and of dislocation cells indicated that dislocations moved individually or in small groups. Schwaiger and Kraft performed a series of fatigue tests of FCC films [49, 50, 51, 52] with film thicknesses ranging from 3.0 μm to 0.2 μm . Their results show that surface extrusions and voids at the film/substrate interface dominate fatigue damage, and that the fatigue lifetime increases with decreasing film thickness. The Si/Cu interface with the Cu-layer thickness of 20 nm is subjected to the cyclic load with the load ratio of $P_{\min} / P_{\max} = 0$ (P_{\min} :

minimum load, P_{\max} : maximum load) [53] (Sumigawa, et al., 2010c). The fatigue process and the fatigue failure is observed in nanometer scale metal. However, the method cannot do tension/compression loading and fatigue in long term beyond 10^7 cycles.

A method using the resonant vibration of specimens has some advantages as compared to previous methods for small materials: the resonant testing do not needs an actuator for a special purpose and some small apparatuses for specimen gripping, residual stress does not exist in the specimen, and completely-reversed cyclic loading is realized without contact. Furthermore, since the method is not affected by slight misalignments in the loading direction, the loading mechanism becomes relatively simple and easy to use. The smaller sample thus can be tested easily.

Contents of this paper

Chapter 2: Anisotropic elastic properties of chiral sculptured thin films at micro-scale evaluated by resonance frequency spectra

Sculptured thin films (STFs) are compose of numerous parallel nano-scale spring-units that have helicoid, zigzag, pillar, and other shapes. Accordingly, for engineering purposes, a micro-size STF is a unidirectional and anisotropic module that can be used in vibration, wave, and acoustic micro-devices at low (less than 1 MHz) and high (more than 100 MHz) frequencies, which depend on material, geometric characteristics of unit element and structural features of the entire film. A multi-section STF can be conceived of as a micro dynamic component that can be integrated with electronic circuitry on a microchip [54,

55].

The new sub-micro dynamics test method is used to excite and measure the vibration of STFs comprised of helical nano-springs with thickness 1.0 μm . In study, two specimens with surface areas of $30 \times 30 \mu\text{m}^2$ and $15 \times 15 \mu\text{m}^2$, respectively, are prepared. Additional mass would be put in a certain place of the specimens, which would change the resonance frequency of specimens and be a significant marker for laser focusing. With this method, the resonance frequencies at the vertical and lateral directions are detected, which make it possible to successfully measure the elastic constants of the STFs.

Chapter 3: Size dependence of fatigue damage in sub-micrometer single crystal gold

In bulk metals under fully-reversed and high-cycle loading, the extrusion/intrusion, of which stress concentration causes crack initiation, appears on the surface. The extrusion/intrusion is formed along a persistent slip band (PSB), which has an understructure of self-organized dislocations with a thickness of a few micrometers. For components smaller than a few micrometers, there is insufficient space to form a PSB and the dislocation structures during fatigue.

PSB-like dislocation structures are not observed in cyclically deformed polycrystalline metal films with sub-micrometer thickness [56], whereas bulk-like features are observed in polycrystalline materials with dimensions of more than a few micrometers [57]. Although these studies have pointed out quite different fatigue behavior in small dimensions from those of bulk materials, these results included the influences of not only specimen size but also

microstructure size. In order to understand the behavior, the influences must be separately inquired [58].

The new sub-micro vibration method is used to investigate the high-cycle fatigue behavior of small specimens. Resonance Vibration fatigue experiments were conducted on single crystal gold cantilevers with different sized sections fabricated by the FIB process. Extrusion/intrusion with width of several hundred, decade and nanometers was identified, which is much narrower than it in the bulk, and the size dependence of the characteristic feature of fatigue damage in micro and sub-micrometer metal components are clarified by this experiment.

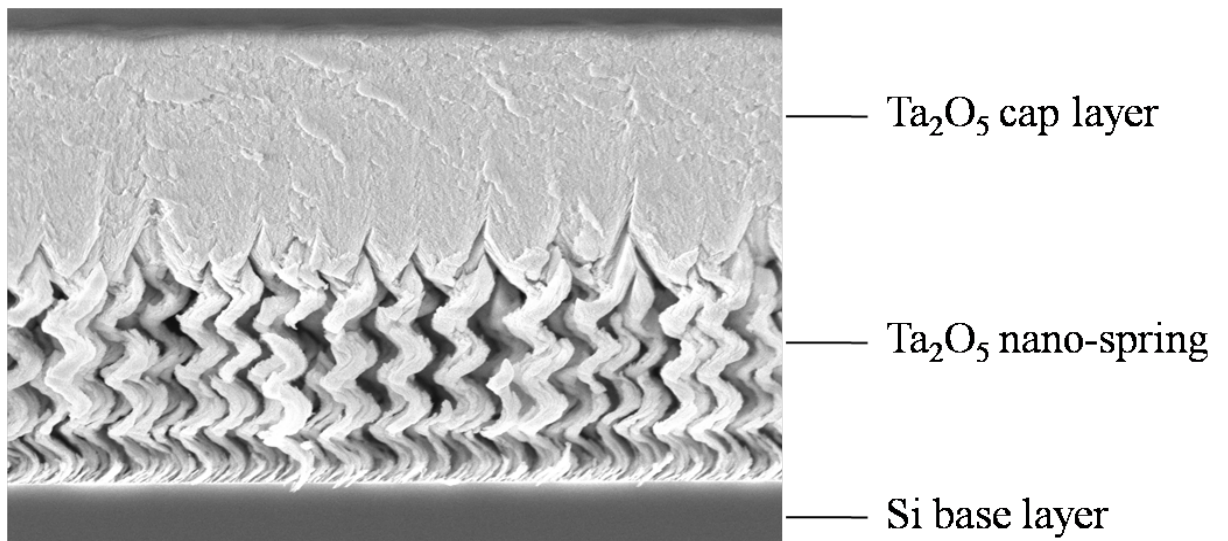
Chapetr 4: Formation of Slip Bands in Nano-polycrystalline Copper under High-Cycle Fatigue of SiTiCuSiN Nanoscale Material

To investigate the effects of a nano-scale stress-field on fatigue damage in a nano-copper component under fully-reversed and high-cycle loading, the resonant fatigue experiment is carried out for a cantilever micro-specimen that has a polycrystalline nano-Cu sandwiched by Si, Ti and SiN. Crystallographic slip bands associated with extrusion/intrusion of about 30 nm width, which is much finer than that in the bulk copper ($\approx 1\mu\text{m}$), are formed on the Cu surface owing to the high-cycle fatigue loading. The new finding, the ultra-fine extrusion/intrusion, suggests existence of different fatigue damage mechanism in the nano-Cu from that in a bulk counterpart. The slip bands appear only in a particular grain though some others possess slip systems with higher Schmid factor. Detailed stress analysis, taking into account the Cu grains and surrounding dissimilar materials (Si, Ti, SiN), indicates that they are formed at a slip system with the highest resolved shear stress, which is in nano-scale. The

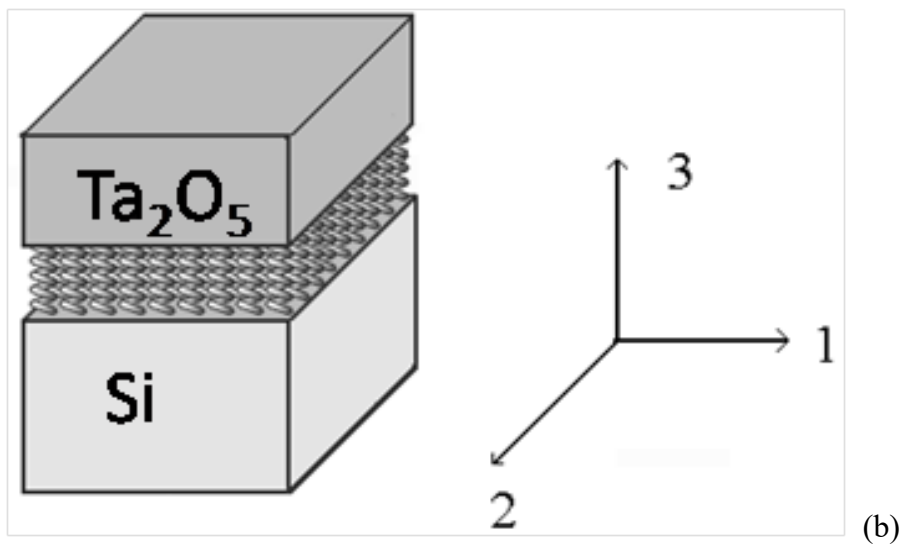
formation stress is much higher than that in a bulk.

Finally, Chapter 5 summarizes the dissertation. Small components often exhibit characteristic mechanical behavior different from those of bulk counterparts. In this dissertation, a new methodology utilizing resonance vibration is developed. A series of experimental studies on the mechanics of their elastic and fatigue behaviors in the micron and submicron-components. In the experiments, the anisotropic elastic properties of chiral sculptured thin films at micro-scale is evaluated, the fatigue damage in sub-micrometer single crystal gold is related to changes in internal length scales, and the slip bands in nano-polycrystalline copper under high-cycle fatigue is readily observed.

Chapter 2: Anisotropic elastic properties of chiral sculptured thin films at micro-scale evaluated by resonance frequency spectra



(a)



(b)

Fig. 1. Sculptured thin films that consist of Ta_2O_5 helical nano-springs formed by dynamic oblique deposition technique: (a) SEM image, and (b) schematic illustration of the thin film with the associated co-ordinate system.

Table 1 Size of Ta₂O₅ nano-springs

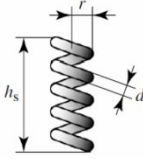
| n | h_s (nm) | r (nm) | d (nm) | N_s (No./ μm^2) | illustration |
|-----|------------|----------|----------|-------------------------------|---|
| 4 | 1030 | 126 | 93 | 15 |  |

Figure 1 shows a field emission scanning electron microscope (FE-SEM) (Hitachi, S-5500) image of STF which consists of tantalum oxide (Ta₂O₅) helical nano-springs. The nano-springs are grown on the Si substrate by the DOD technique using the electron beam (EB) evaporation. The incident angle, defined as the one between the incident flux and the normal to the substrate, is set at 87°, and the substrate is rotated during the deposition so that the number of turns n is 4. Nano-springs, which have almost identical shape in the film, are isolated from each other as shown in Fig. 1. The diameter of spring wire d gradually increases from bottom to top, which is a characteristic feature often observed in the nano-springs manufactured by DOD. The average size of nano-springs is listed in Table 1. Here, N_s is the number of nano-springs contained in a unit area, and h_s , r , and d are the scale of spring as illustrated in Table 1. A Ta₂O₅ cap layer with a thickness of $h_c = 1030$ nm is deposited by the EB evaporation after the growth of nano-springs. Thus, the sculptured thin film of nano-springs is sandwiched between the Ta₂O₅ cap and Si base layers. Since the in-plane symmetry of the film dictates, the linear elastic constant matrix is in the form

$$\mathbf{C} = \begin{bmatrix} c_{11} & c_{12} & c_{13} & 0 & 0 & 0 \\ c_{12} & c_{11} & c_{13} & 0 & 0 & 0 \\ c_{13} & c_{13} & c_{33} & 0 & 0 & 0 \\ 0 & 0 & 0 & c_{44} & 0 & 0 \\ 0 & 0 & 0 & 0 & c_{44} & 0 \\ 0 & 0 & 0 & 0 & 0 & c_{66} \end{bmatrix}, \quad (1)$$

In addition, another key structural feature is in-plane discreteness. Because there is almost no contact between two neighboring springs, $c_{11} \approx 0$, $c_{12} \approx 0$, $c_{13} \approx 0$ and $c_{66} \approx 0$. Then, the linear elastic constant matrix is

$$\mathbf{C}_{film} = \begin{bmatrix} 0 & 0 & 0 & 0 & 0 & 0 \\ 0 & 0 & 0 & 0 & 0 & 0 \\ 0 & 0 & c_{33} & 0 & 0 & 0 \\ 0 & 0 & 0 & c_{44} & 0 & 0 \\ 0 & 0 & 0 & 0 & c_{44} & 0 \\ 0 & 0 & 0 & 0 & 0 & 0 \end{bmatrix}. \quad (2)$$

The vertical stiffness k_v and lateral stiffness k_l of single nano-spring are obtained from the following equations:

$$k_v = \frac{c_{33} \times S}{h_s} \times \frac{1}{N_s \times S}, \quad (3-1)$$

$$k_l = \frac{c_{44} \times S}{h_s} \times \frac{1}{N_s \times S}, \quad (3-2)$$

where S is area of thin film. The density ρ_{film} of thin sculptured films is given by

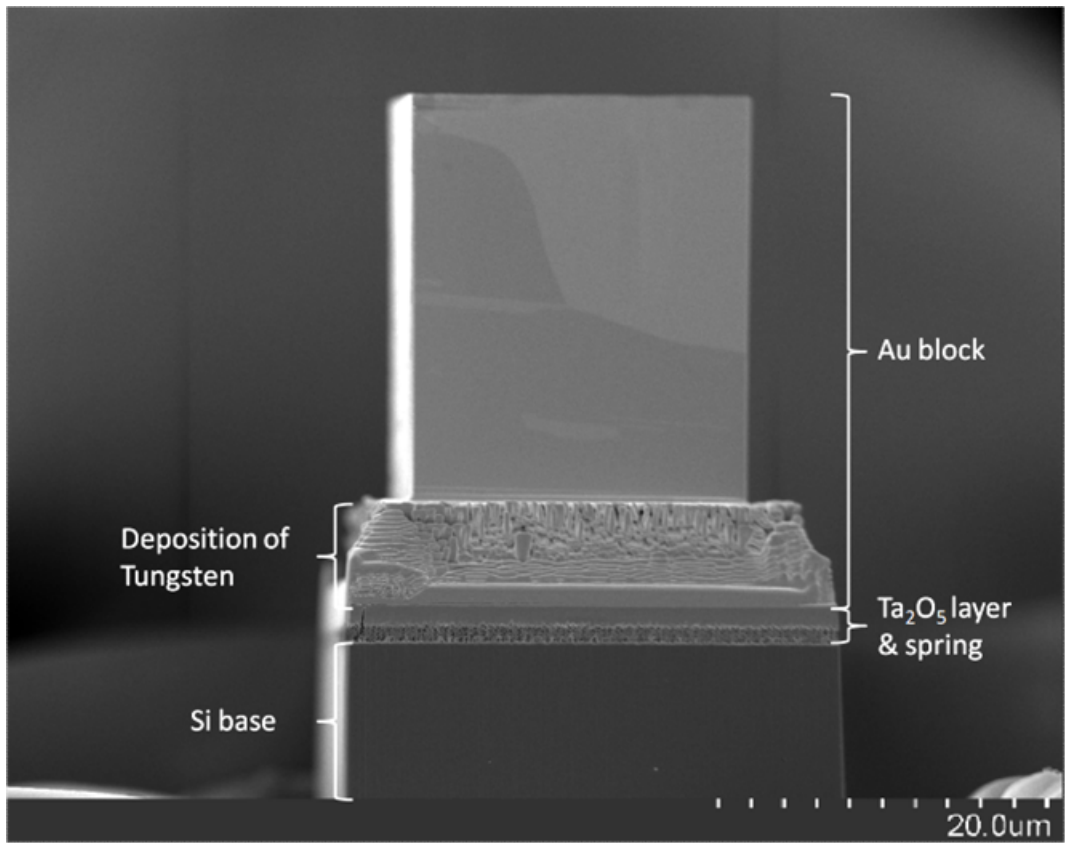
$$\rho_{film} = \rho_{Ta_2O_5} \times \pi \left(\frac{d}{2} \right)^2 \times 2\pi r \times n \times N_s, \quad (4)$$

where $\rho_{Ta_2O_5}$ is the density of Ta_2O_5 .

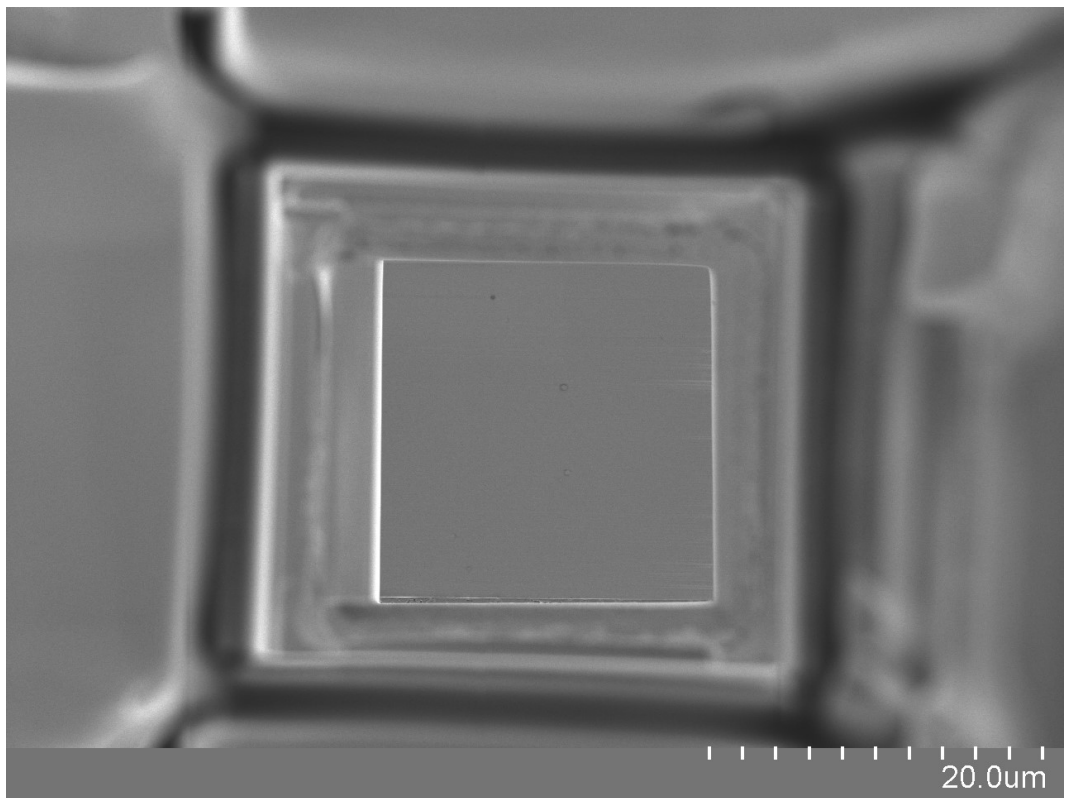
2.1 Experimental and analytical procedure

2.2.1 Specimen preparation

We prepare two specimens with design of $30 \times 30 \mu\text{m}^2$ (specimen A, FE-SEM image shown in Fig. 2) and $15 \times 15 \mu\text{m}^2$ (specimen B, FE-SEM image shown in Fig. 3) respectively, which are cut by means of a focused ion beam (FIB) processing system (Hitachi, FB-2200). Because, a nano-scale component (Fig. 4(a)) usually have a resonant frequency of GHz order, it is very difficult to achieve the precise measurement. In order to reduce the resonant frequency, we need to increase the mass, as shown in Fig. 4(b). We add Au-block on the thin films by means of the FIB system, which is fixed on the Ta_2O_5 cap layer by deposition of Tungsten as shown in Figs. 2 and 3. The added mass is expected to decrease the resonance frequency to MHz order. Because the nano-springs layer of sculptured thin films is soft and the Au block is “very heavy”, the specimen could have a 3-DOF vibration under a harmonic excitation along the axis. This means that there appear several main modes in the resonance spectra (Friswell and Mottershead, 1995). The number of main modes depends on the direction of excitation. The dimensions of the specimens used for evaluating the elastic properties of the sculptured thin films are listed in Table 2.

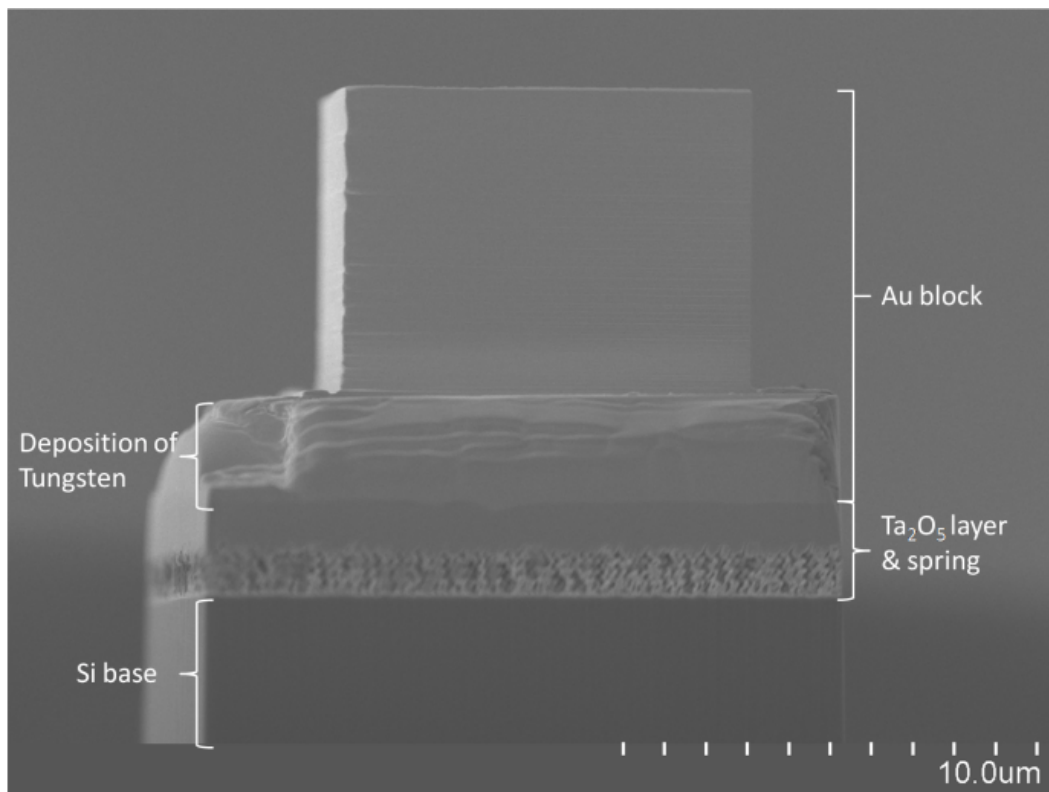


(a)

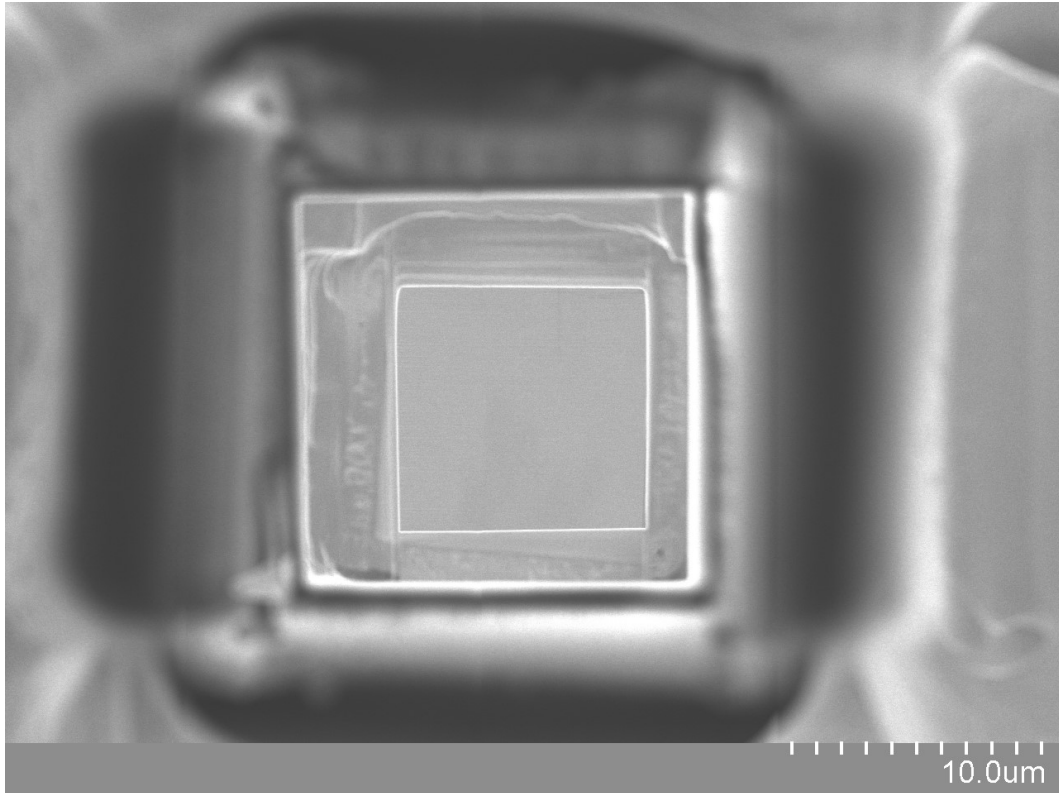


(b)

Fig. 2 Specimen A for evaluating the elastic properties of the sculptured thin films, Specimen configuration; specimen is a brick consisting of a Au block (top view surface measuring $20 \times 20 \mu\text{m}^2$), a Ta_2O_5 cap layer (top view surface measuring $30 \times 30 \mu\text{m}^2$), a nano-springs layer, and a Si base layer; brick is fabricated from multilayered thin films by FIB. (a) side view, (b) top view.



(a)



(b)

Fig. 3 Specimen B for evaluating the elastic properties of the sculptured thin films, Specimen configuration; specimen is a brick consisting of a Au block(top view surface measuring $10 \times 10 \mu\text{m}^2$), a Ta_2O_5 cap layer(top view surface measuring $15 \times 15 \mu\text{m}^2$), a nano-springs layer, and a Si base layer; brick is fabricated from multilayered thin films by FIB. (a) side view, (b) top view.

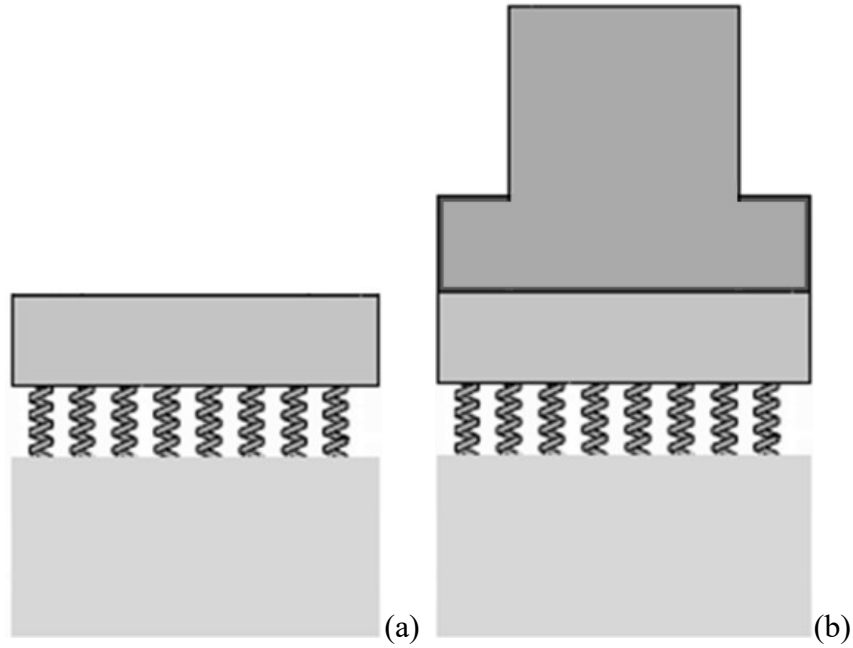


Fig. 4 Schematic of components without Au block (a) and with Au block (b).

Table 2 Dimensions of the specimens used for evaluating the elastic properties of the sculptured thin films

| Specimens | b_{au} (μm) | b_c (μm) | h_{au} (μm) | h_t (μm) | h_c (μm) | h_s (μm) | illustration |
|-----------|-------------------------------|----------------------------|-------------------------------|----------------------------|----------------------------|----------------------------|--------------|
| A | 20 | 30 | 30 | 6.18 | 1.03 | 1.03 | |
| B | 10 | 15 | 10 | 2.65 | 1.03 | 1.03 | |

2.2.2 Experiment equipment facilitation

The system assembled is shown schematically in Fig. 5. The specimen is affixed with a piezoelectric actuator, which provides a frequency sweep vibration (Dc: 0 Hz to 40 MHz) by using signal generator (Polytec: MSA-500 Processing

Unit). This enables us to excite lateral or vertical vibration to the STF. The actuator is mounted on an X–Y–Z stage so that it can make relative movement for the spectra measurement. To minimize extraneous vibrations, the system is mounted on a vibration isolation table. The vibrational response of specimen is monitored using a laser Doppler vibrometer (LDV) (Polytec: MSA-500), which can measure displacement over a frequency range of 0 Hz–24 MHz.

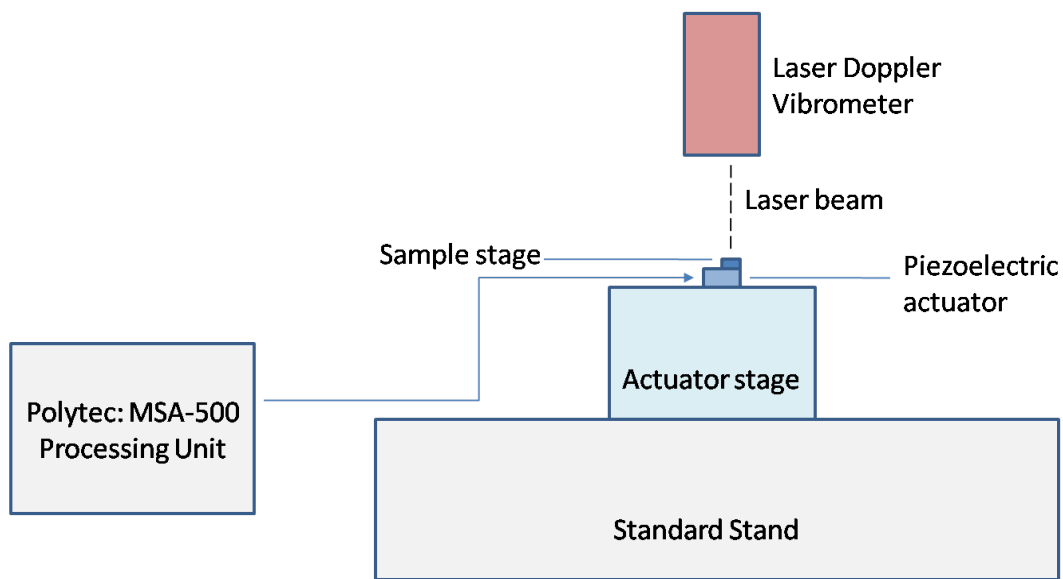
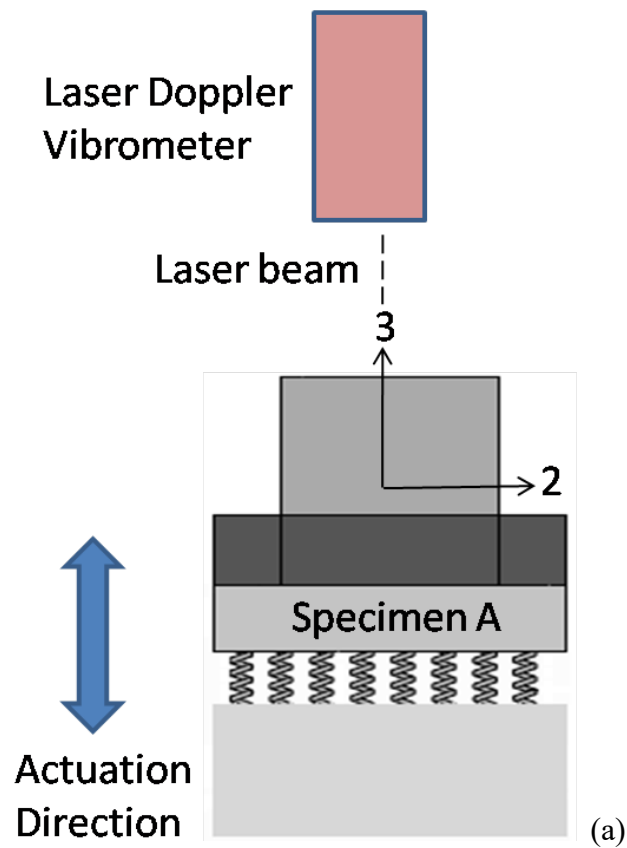


Fig. 5 Schematic representation of Frequency-Sweep Vibration system based on Laser Doppler.

2.2.3 Testing condition

To evaluate the elastic property of thin film, resonance frequencies under different modes must be measured: in this study, the vertical (axis 3) and lateral (axis 2) vibrations of specimens are actuated at room temperature as shown in Fig. 6 (a) and (b). The Si substrate of specimen A is actuated vertically, and the vertical displacement (the axis 3 in the specimen coordinate system) at the top surface is measured, which is designated as “task one” (Fig. 6(a)) in the paper. Si substrate of specimen B would be actuated laterally, and the lateral displacement

(the axis 2) at the side surface is measured, which is designated as “task two” (Fig. 6(b)). Tasks one and two are designed for identifying the elastic property c_{33} and c_{44} . For examining the reliability of elastic property obtained, “task three”, where the specimen B is actuated laterally again and the vertical displacement (the axis 3) at the top surface is measured, is conducted (Fig. 6(c)).



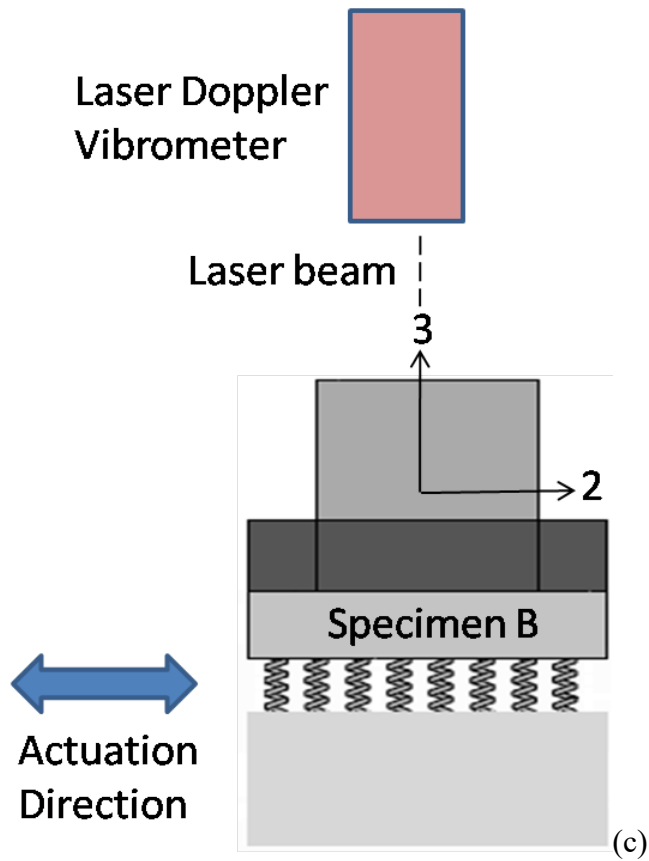
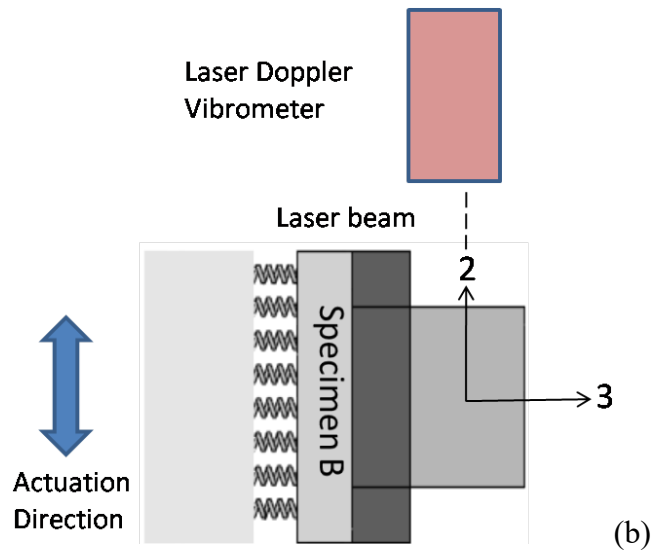


Fig. 6 Schematic of tasks: (a) task one, (b) task two, (c) task three.

2.2.4 Numerical analysis

Numerical analysis is conducted using a commercial software of finite element method (FEM), ABAQUS 6.5-1. Figures 7(a) and (b) show the finite

element models of specimen A (model A) and specimen B (model B), respectively. The configuration is constructed based on the 3D image of SEM micrographs. Because the Si substrate is a “giant” solid compared with the specimen, the deformation of substrate can be neglected. Then, the substrate is treated as a 3D analytic rigid shell. The STF is treated as an orthotropic elastic material, and the linear elastic constant matrix and density ($2.38 \times 10^3 \text{ kg/m}^3$) are defined by Eqs. (2) and (4) respectively. The interaction between the Si substrate and the sculptured thin film is defined as surface to surface contact (“rough” tangential and “hard” normal). The Ta₂O₅ cap layer, Tungsten and Au block are treated as 3D deformable solid. The interaction between Ta₂O₅ cap layer and deposited Tungsten is defined as surface to surface contact (“rough” tangential and “hard” normal). Because the deposited Tungsten is non-uniform, the actual interaction is complex. This would cause noise in the experiment. However, since the STF is very soft and the Au block is very “big”, these govern the vibration behavior. We focus on the dominated vibration eliminating the noise in the comparison between the experiment and analytical results.

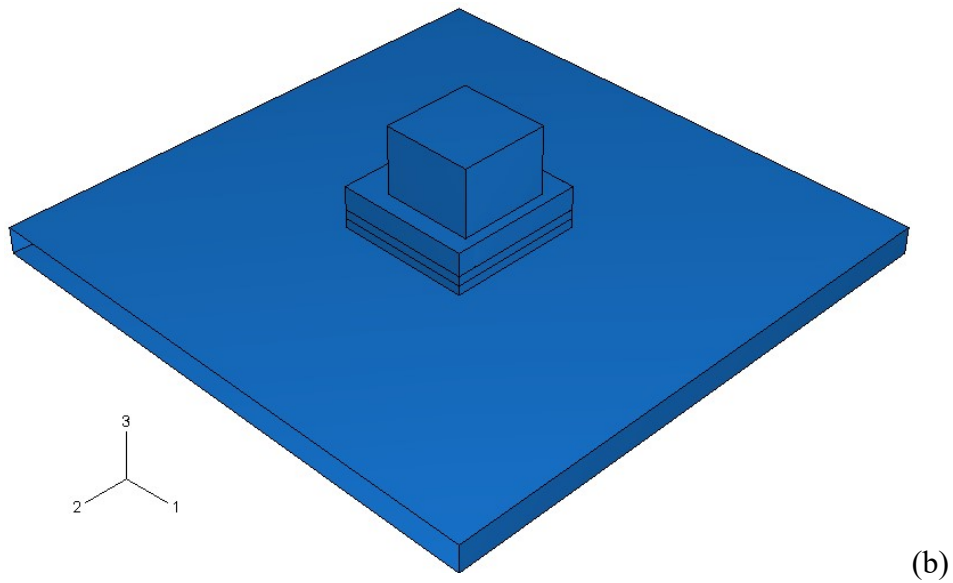
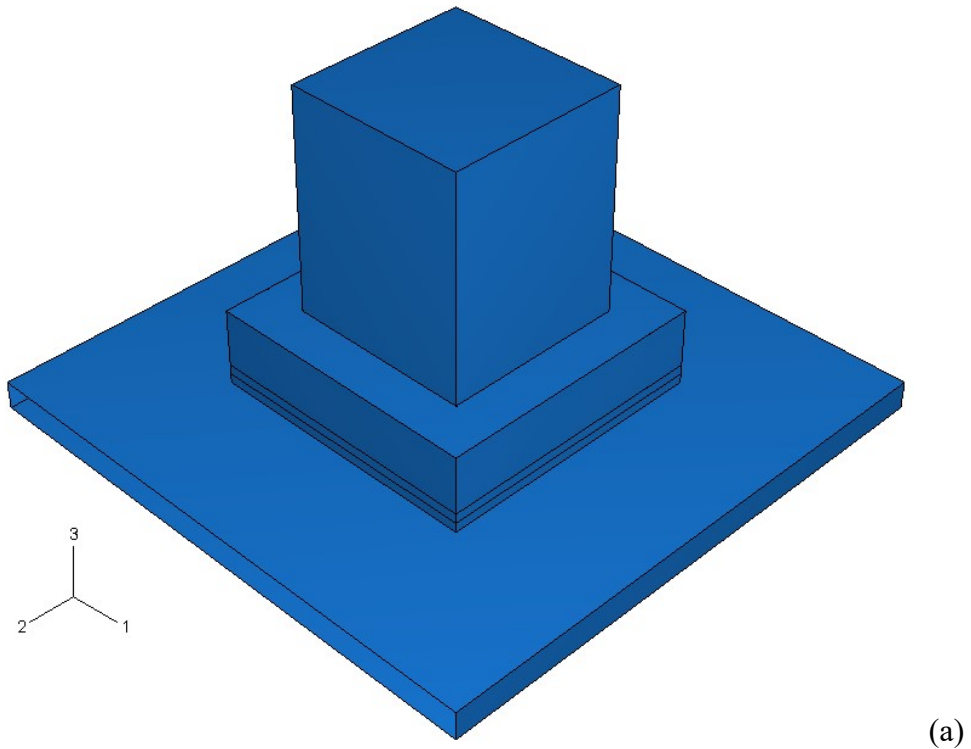


Fig. 7 Typical finite element model: (a) model A, (b) model B

2.2 Results and discussion

2.3.1 Vertical and Lateral elastic property of Sculptured thin film

Task one: Vertical vibration and Vertical elastic property

Since the specimen is small, the displacement is dominated by the

movement of sample stage. Then, it is necessary to compare the swept-frequency spectra of sample stage and specimen for identifying the resonance frequency. Figure 8 shows the swept-frequency spectra observed for specimen (black solid line) and sample stage (red dash line). The Savitzky-Golay method is used to smooth the original data. The peaks around 0.5 MHz overlap each other, which mean the vibration entire sample stage. On the other hand, one significant peak of solid line is found at 1.31 MHz only on the specimen. This is the resonance frequency of vertical vibration. There are some small peaks during 0.5MHz and 2MHz, which include the fixture, spurious or local modes due to the experimental ambiguity.

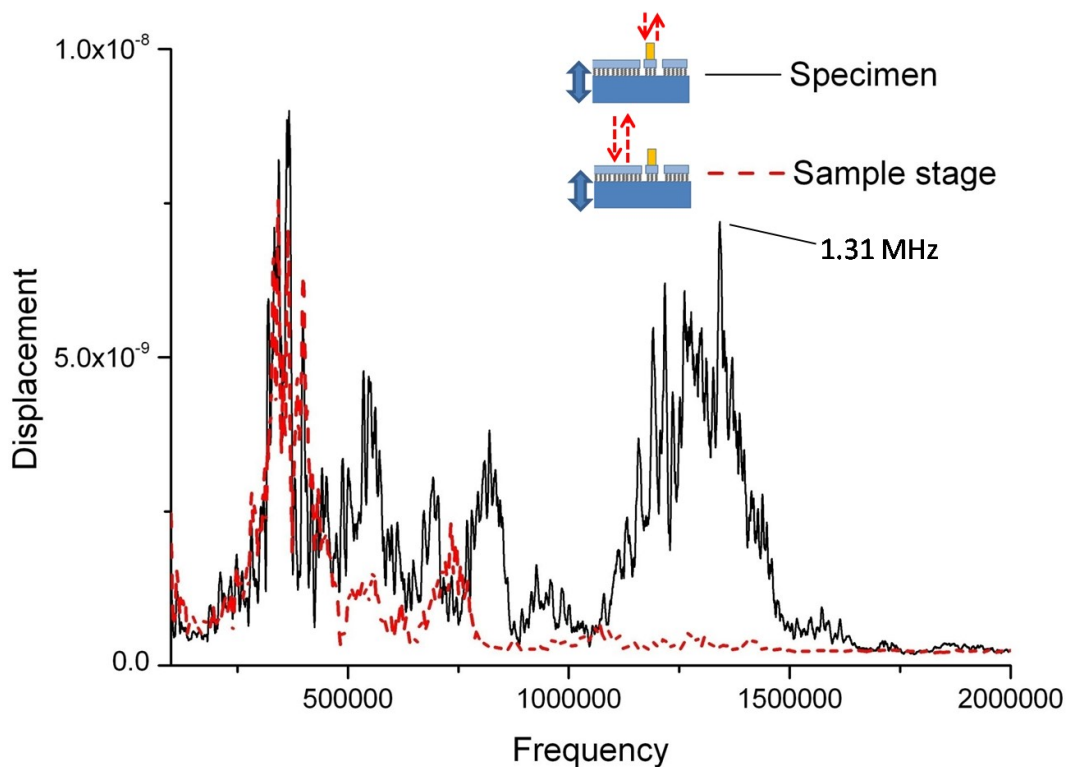


Fig. 8 Task one: swept-frequency spectra of Ta₂O₅ cay layer and specimen

Numerical analysis is conducted on model A (Fig. 7(a)). Because the amplitude of force does not influence the resonance frequency, a vertical load

along the axis 3 with amplitude ($1 \times 10^{-6} N$) is used for the analysis.

At first, we examine the influence of c_{44} on the vertical vibration. It is expected by the shape and size of spring and elastic modulus of Ta_2O_5 that k_v and k_l are in the order of 3~10 N/m and 0.5~3 N/m (Hirakata et al., 2007). Using Eq. (3), c_{33} and c_{44} are in the range of 0.05~0.15GPa and 0.01~0.05GPa, respectively. Figure 9 shows the resonance frequencies obtained by FEM simulation with a constant c_{33} (0.11GPa) and variable c_{44} . As expected, the resonance frequency of vertical vibration is independent of c_{44} . The results are similar for different magnitude of c_{33} .

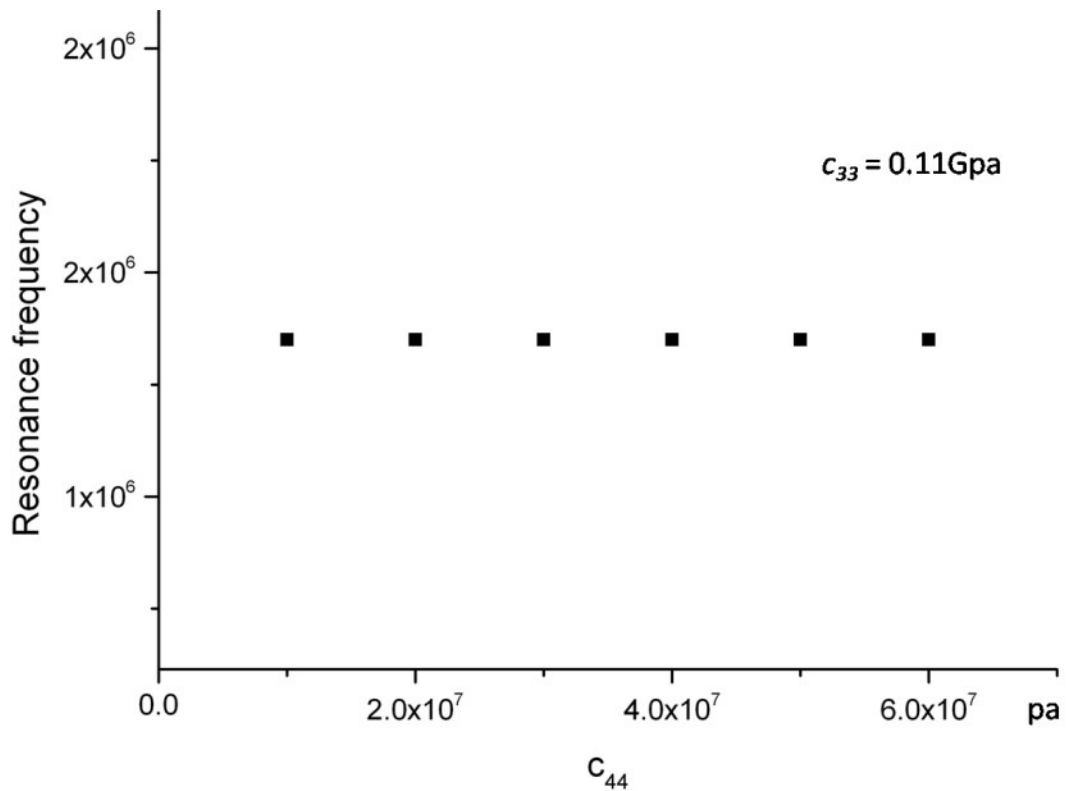


Fig. 9 Illustration of resonance frequencies for constant c_{33} and variable c_{44}

To identify the vertical elastic property, the finite element model is conducted changing the magnitude of c_{33} under $c_{44} = 0.03$ GPa ($k_l = 2.05$ N/m (Hirakata et al., 2007)). The swept-frequency is from 0.5 MHz to 2 MHz. When

c_{33} is between 0.085GPa and 0.090GPa, the resonance frequency is close to the experimental result. When $c_{33} = 0.087$ GPa, as shown in the Fig. 10, the significant peak is 1.33 MHz. Thus, c_{33} is inversely extracted to be $0.087 \times (100 \pm 5)\%$ GPa. k_v can be converted from it by Eq. (3). Although we set different c_{44} and repeat the simulation above, the result changes little.

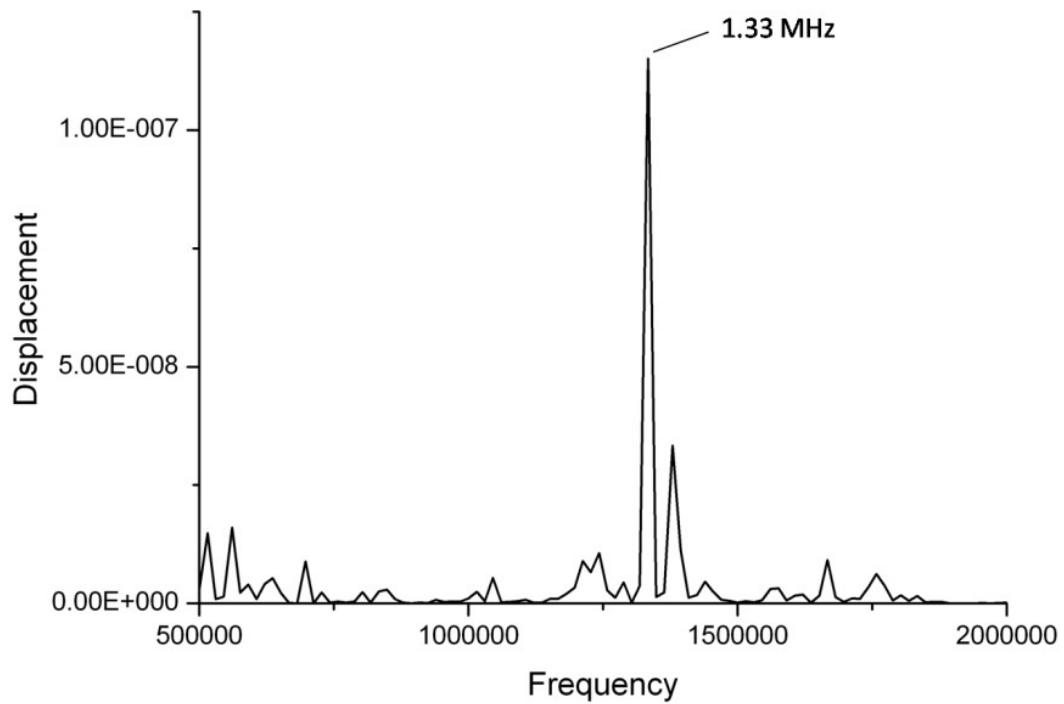


Fig. 10 Task one: Simulation results of specimen

Task two: Lateral vibration and Lateral elastic property

Figure 11 shows the swept-frequency spectra observed on the specimen (black solid line) and sample stage (red dash line). The Savitzky-Golay method is used to smooth the original data. The significant peaks (0.93 MHz and 1.35 MHz) present the resonance frequencies of lateral vibration in the specimen.

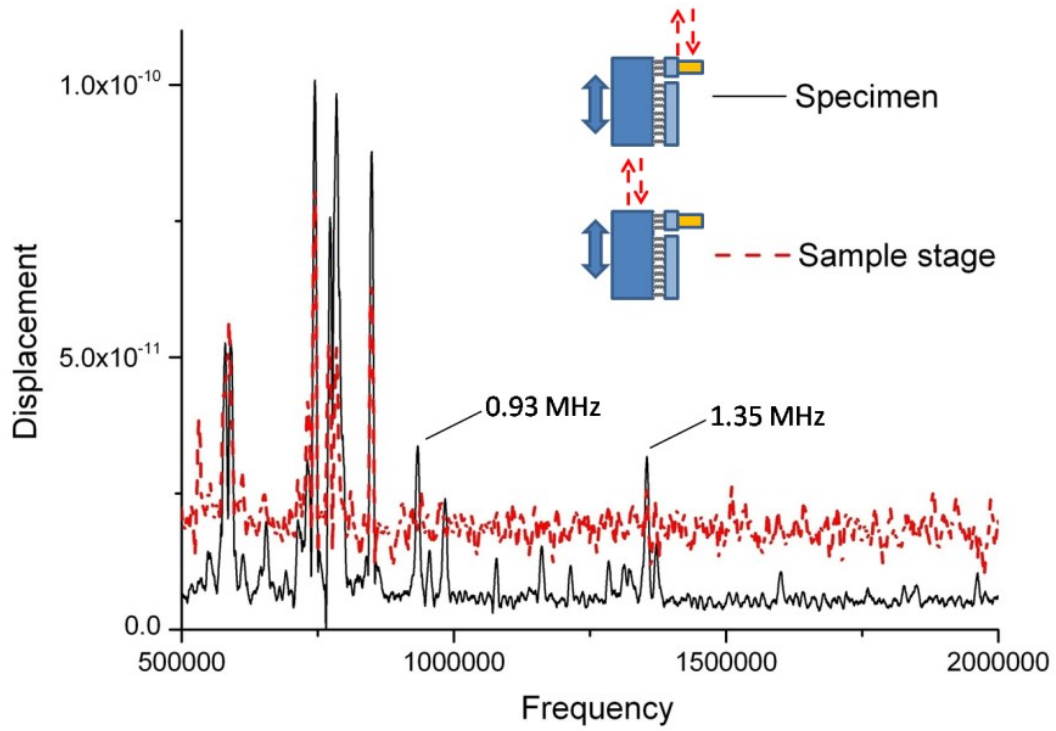


Fig.11 Task two: swept-frequency spectra of Si base and specimen

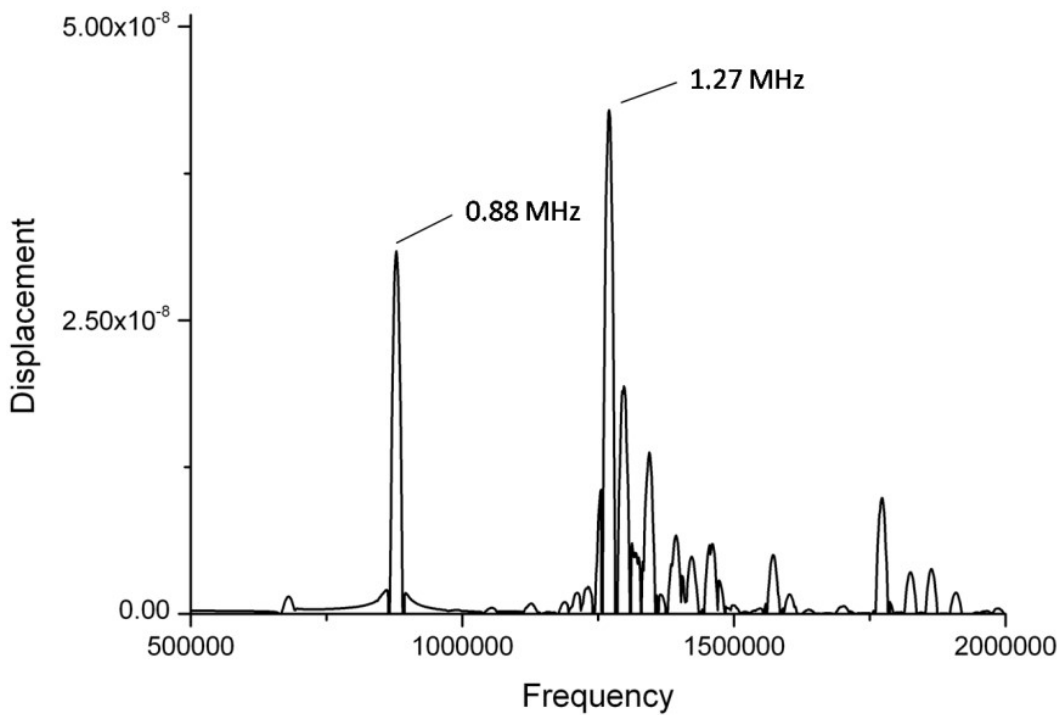


Fig.12 Task two: Simulation results of specimen

To identify the vertical elastic property, the finite element simulation (Fig.

7(b)) is conducted. Changing the magnitude of c_{44} under $c_{33} = 0.087$ GPa, the swept-frequency is applied from 0.5 MHz to 2 MHz. $c_{44} = 0.036$ GPa \sim 0.040 GPa, gives reasonable correspondence of the resonance frequency to the experimental result. Figure 12 shows spectra obtained by the FEM under $c_{33} = 0.087$ GPa and $c_{44} = 0.038$ GPa. The significant peaks are at 0.88 MHz and 1.27 MHz. The elastic property of sculptured thin film and the stiffness of nano-spring are obtained, which are listed in Table 3.

Table 3. The elastic property of this sculptured thin film and the stiffness of nano-spring

| E (GPa) | G (GPa) | K_v (N/m) | K_l (N/m) |
|------------------------------|------------------------------|-----------------------------|-----------------------------|
| $0.087 \times (100 \pm 5)\%$ | $0.038 \times (100 \pm 5)\%$ | $5.63 \times (100 \pm 5)\%$ | $2.45 \times (100 \pm 5)\%$ |

2.3.2 Verification

Figure 13 shows the spectra of vertical vibration obtained from the experiment, task 3 (after the Savitzky-Golay smoothing). It elucidate one significant peak (1.33 MHz). Because the axis 3 is not the main direction of this mode, the vibration amplitude is small.

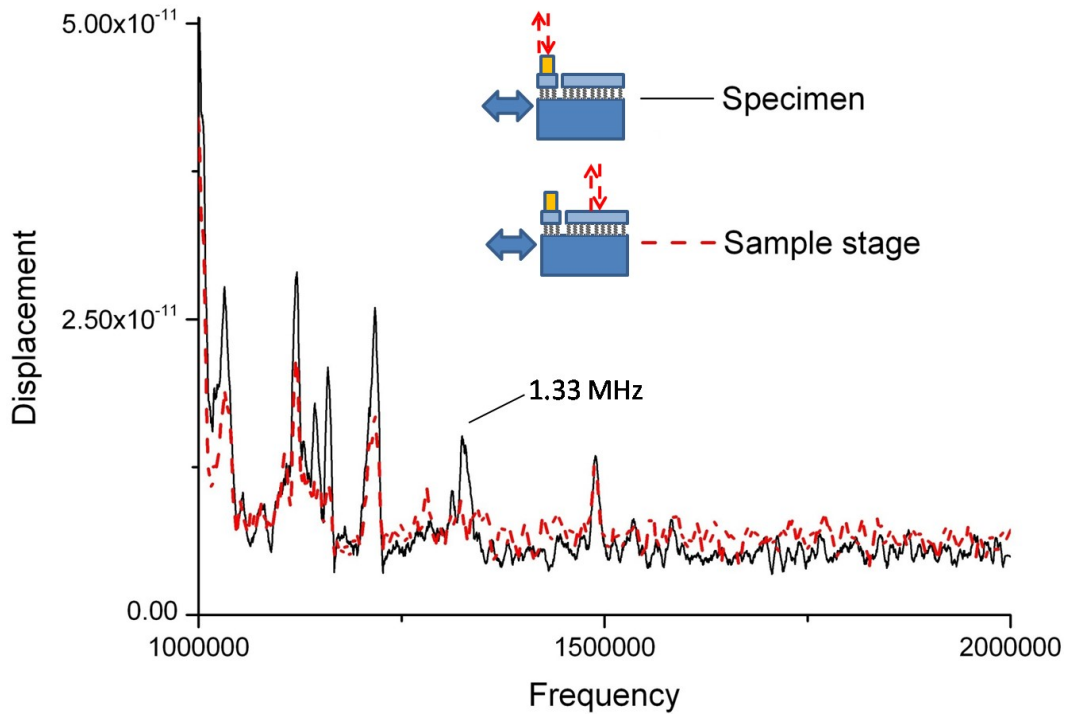


Fig.13 Task three: swept-frequency spectra of Ta₂O₅ cap layer and specimen.

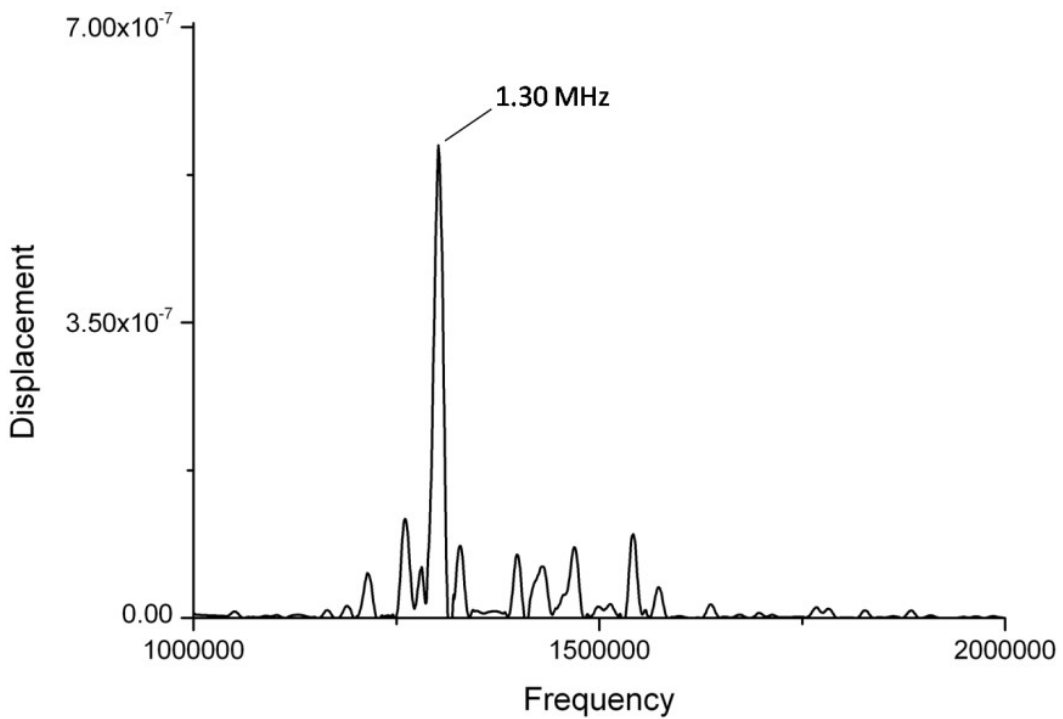


Fig.14 Task three: Simulation results of specimen

To check the magnitudes of c_{33} and c_{44} , the finite element analysis using the

model shown in Fig. 7(b) with $c_{33} = 0.087$ GPa and $c_{44} = 0.038$ GPa is conducted under the sweeping frequency of 1 MHz to 2 MHz. It shows the significant peak at 1.30MHz as shown in Fig. 14, which is close to the experiment results. Based on this task, the elastic property of sculptured thin film is confirmed.

*Chapter 3: Size dependence of fatigue damage in sub-micrometer single crystal
gold*

2. Experimental procedure

2.1. Material and specimen

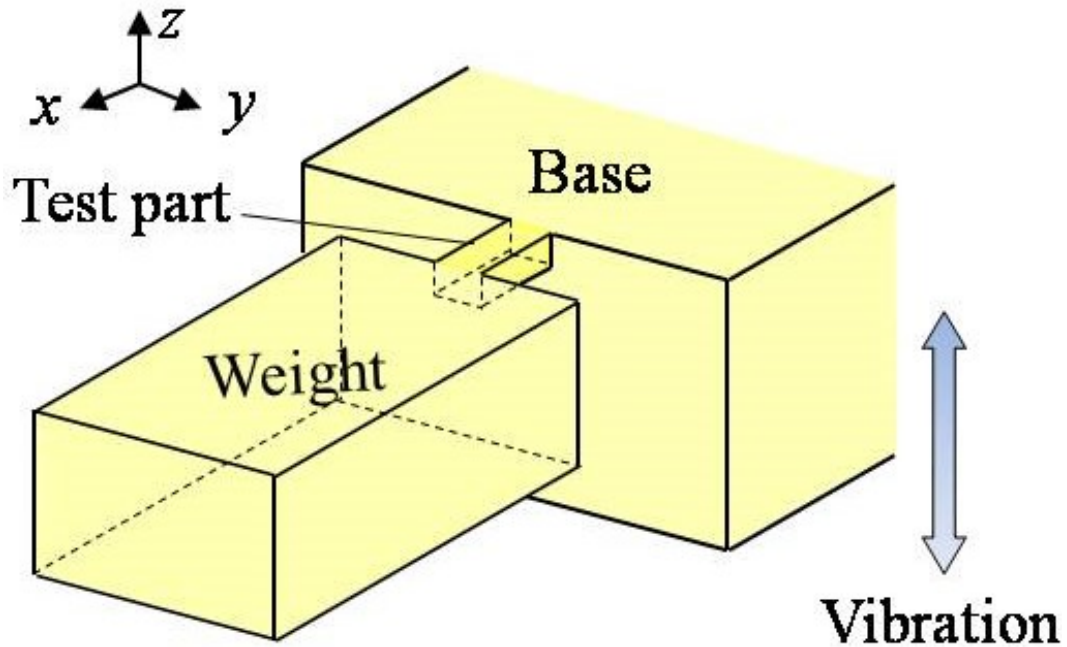
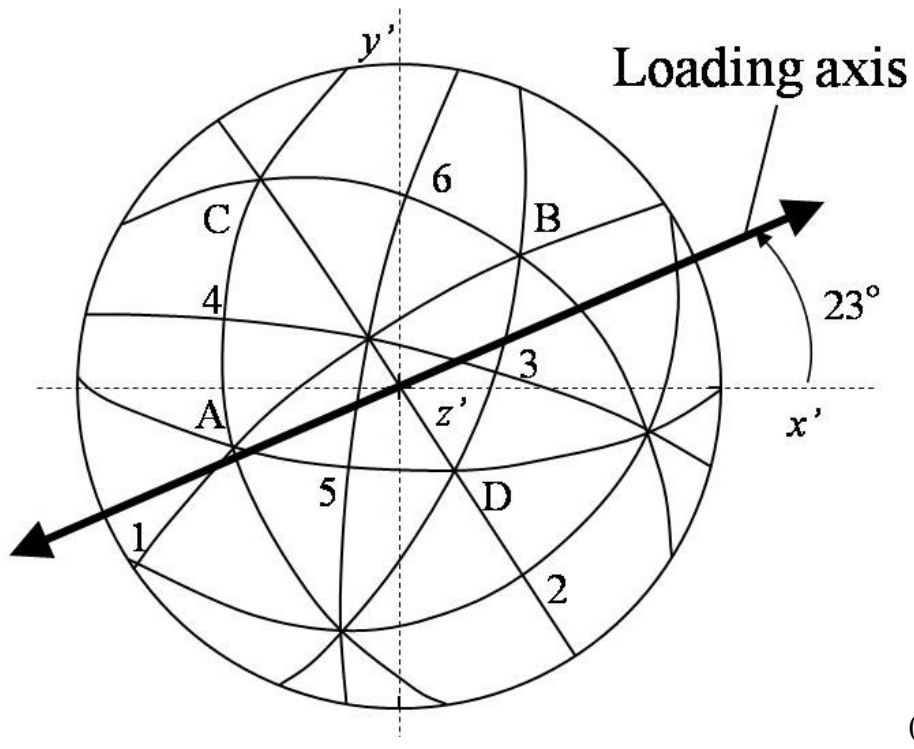
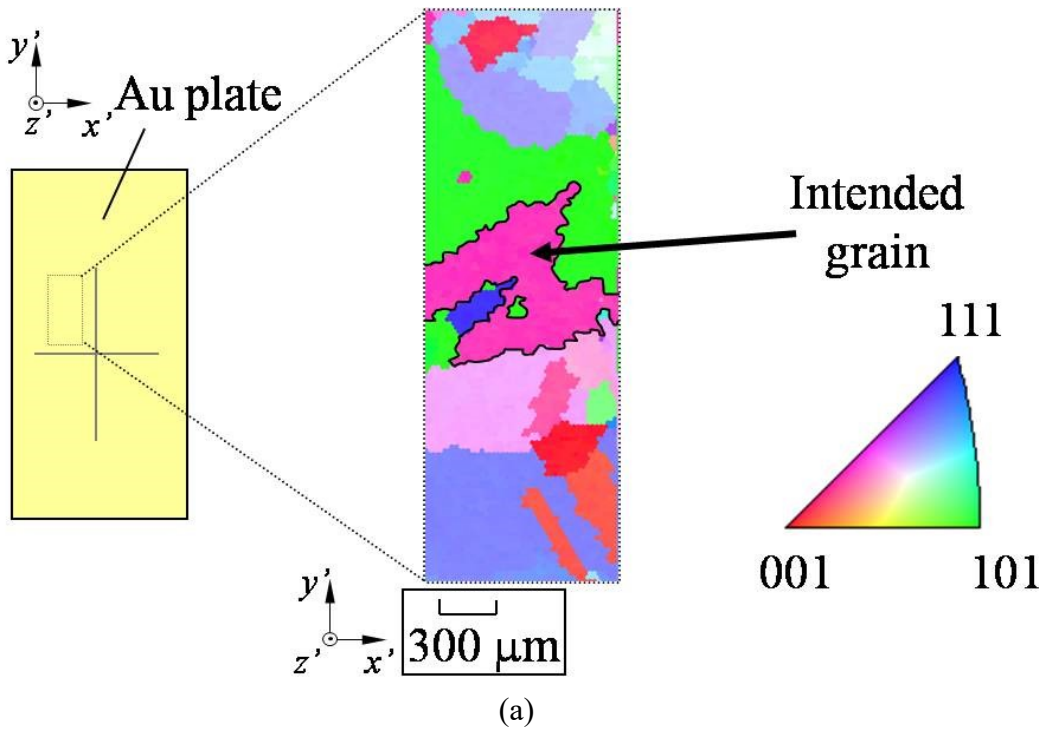


Fig. 1 Schematic illustration of cantilever specimen

Figure 1 shows the schematic illustration of cantilever specimen with the weight. Here, the base of specimen is actuated, and the bending resonant vibration in the vertical direction is applied. As submicron component generally has a resonant frequency of over a few tens of GHz, it is difficult to control the fatigue cycle. To reduce the resonant frequency of the test section, a weight is added on the specimen tip [22].



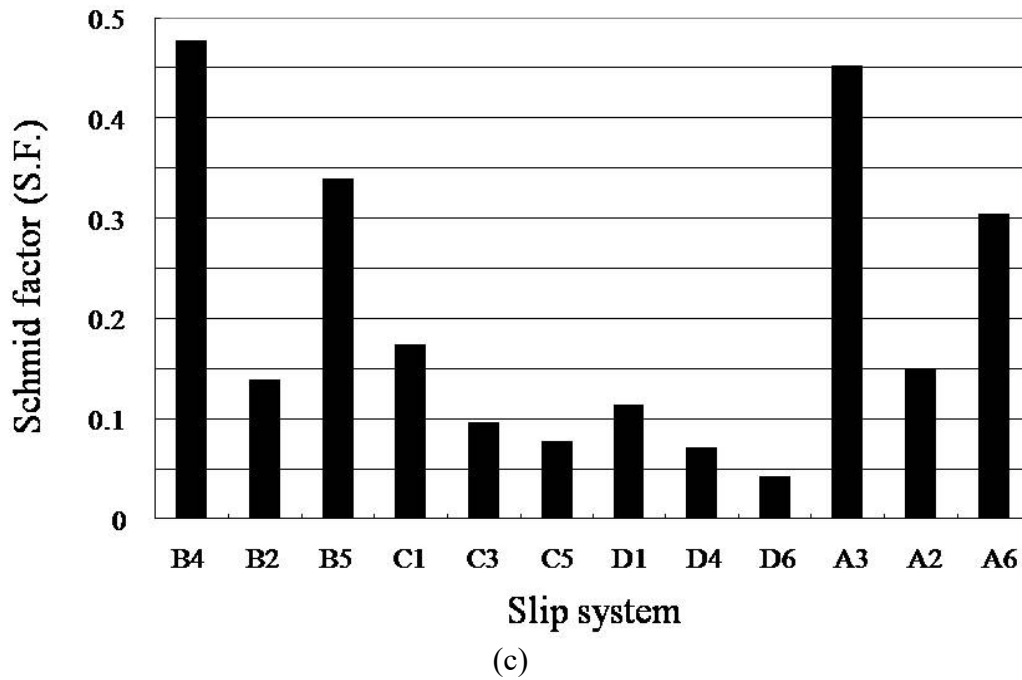


Fig. 2 EBSD map of gold plate (a), stereographic projection of the selected grain (b) and Schmid factor (S.F.) on the slip system of the selected grain (c)

The specimens are made by the following process:

(a) A gold single-crystal block is cut by mean of a focused ion beam (FIB) processing (Hitachi, FB-2200; accelerating voltage: 40 kV) from a crystal in a polycrystalline plate (purity: 99.95%; mass density: $19.3 \times 10^3 \text{ kg/m}^3$) after annealing in vacuum ($4.0 \times 10^{-4} \text{ Pa}$) at 1073 K for 24 h to remove residual stress (Fig. 3a). The crystal orientation and shape of each grain in the gold plate are identified by the electron backscatter diffraction before the selection of crystal (Fig. 2a). The x-axis of cantilever specimen is along the loading axis as shown in Fig. 2b.

(b) The block is picked up by a microprobe. (Fig. 3b)

(c) The bottom surface of block is processed so that it becomes parallel to

the upper surface. The block is mounted on a silicon (Si) plate by tungsten (W) deposition. The block (weight) is formed on the cantilever (test section) tip. (Fig. 3c)

(d) The damaged layer on the surface, which has been produced by the FIB, is removed by argon (Ar) ion milling. (Fig. 3d)

The slip planes and directions in the gold single crystal specimen are labeled by the combination of planes A–D and directions 1–6 as shown in the Fig. 2b. Figure 2c shows the Schmid factor (S.F.) on the slip system of this grain. The B4 slip system has the maximum resolved shear stress with the S.F. of 0.47.

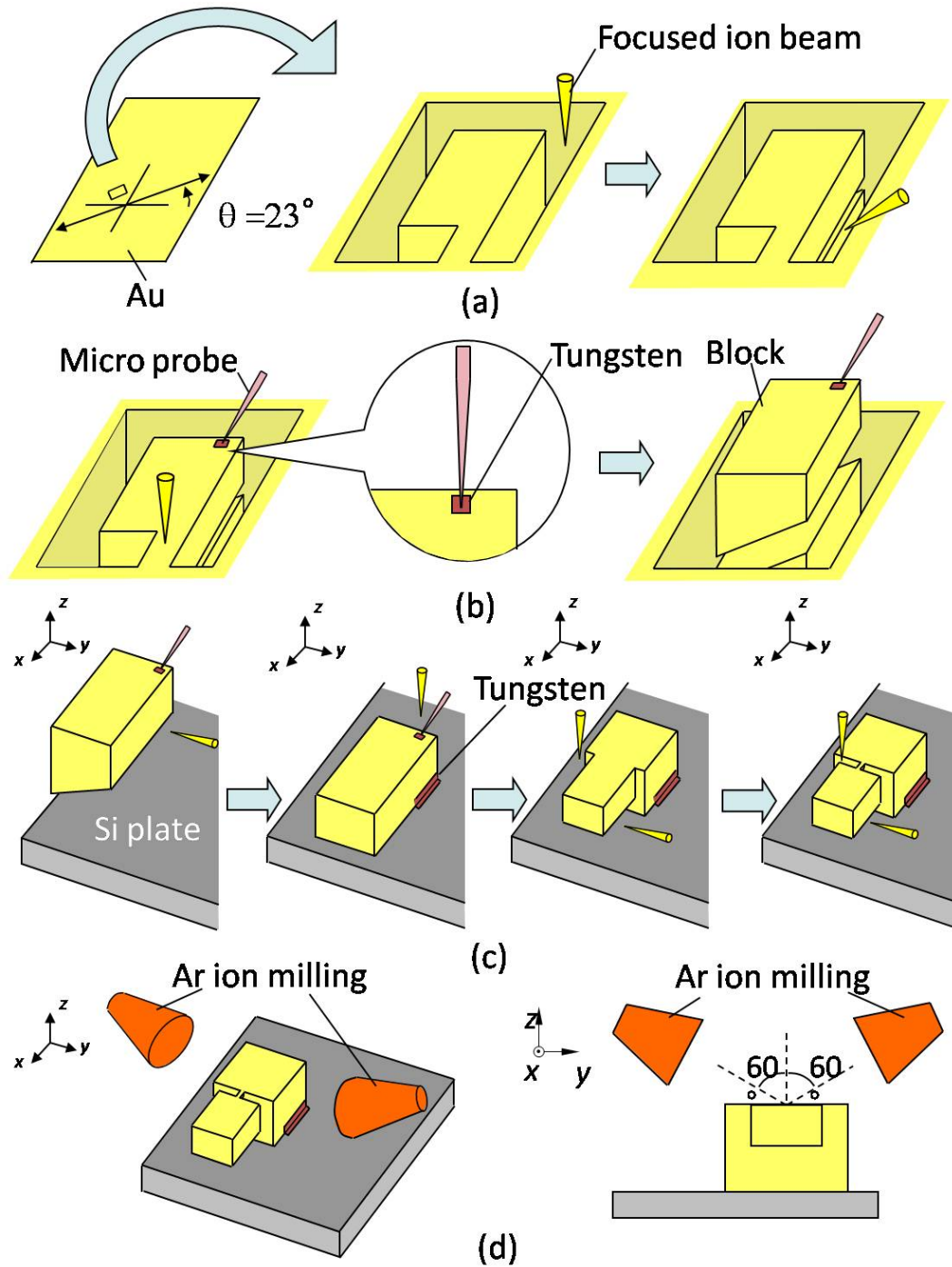
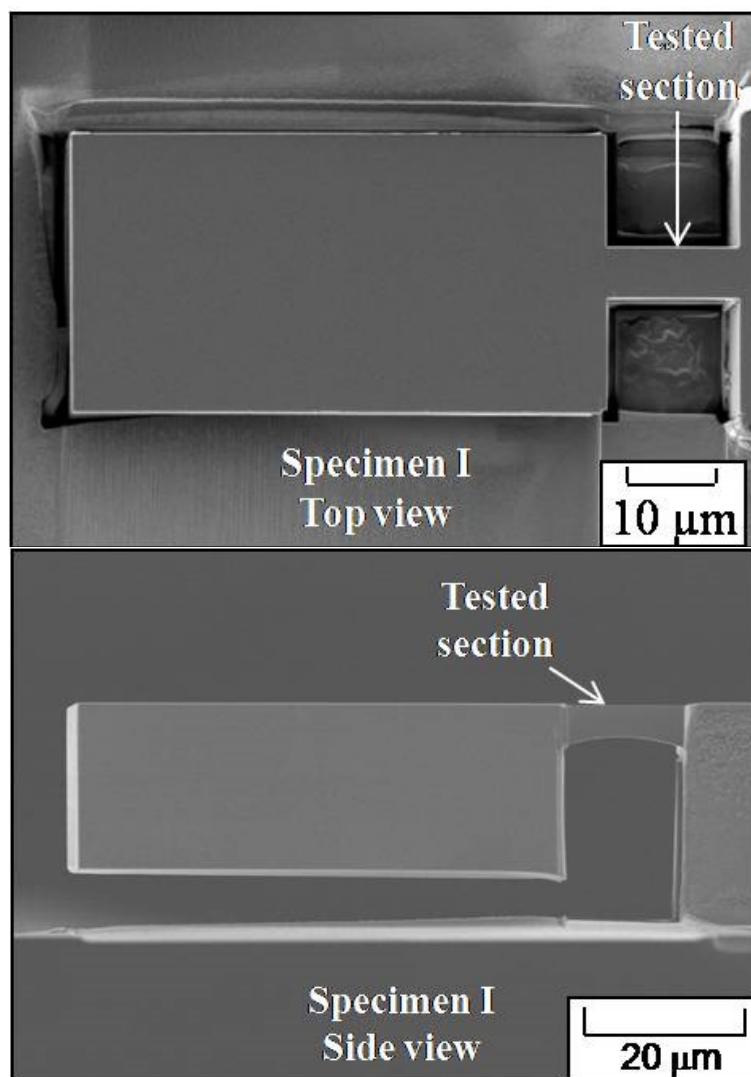


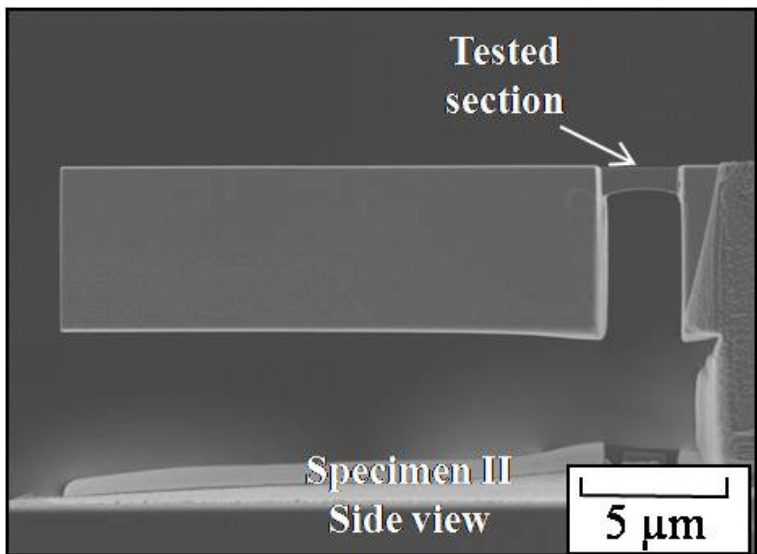
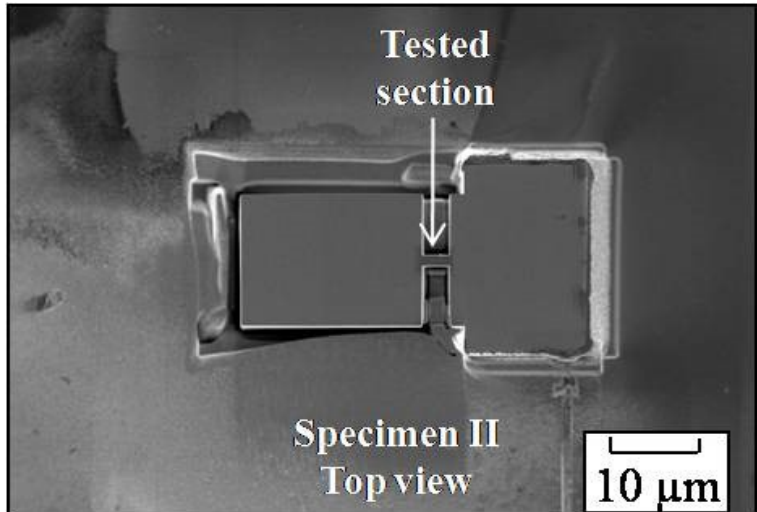
Fig. 3 Schematic illustration of FIB processing of specimen

Three specimens with different size are prepared as shown in Fig.4 (a, b, c). Schematic illustration of geometry of specimens is shown in Fig.4 (d, e), and the sizes of specimens are listed in Table 1, where w , h , l and R are the width, height,

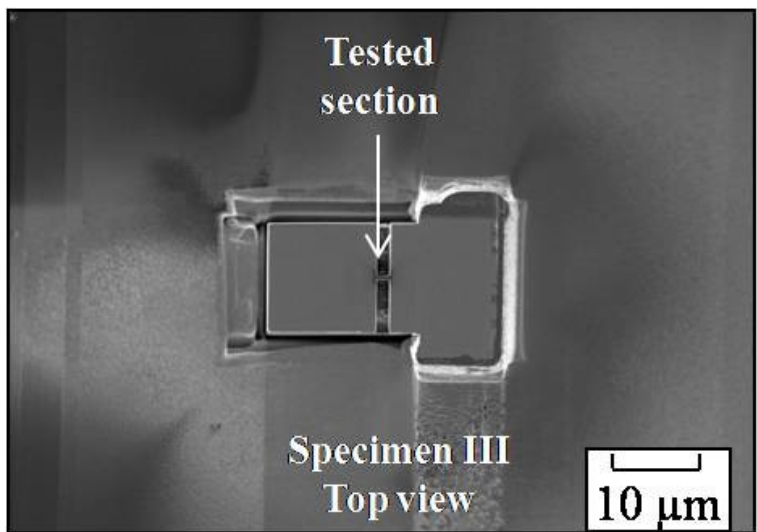
length of cantilever, and radius of circular of test section, and W , H , and L are the width, height and length of weight block, respectively. The specimens have same crystallographic orientation, of which stereographic projection of the specimens is shown in the Fig. 2b. Since the vertical resonant frequency of the specimen, f_0 , is approximately proportional to $m^{-1/2}$ and $l_c^{-3/2}$ (m : the mass, l_c : the distance from the test section to the gravity center of the weight), the specimens have $f_0 < 100$ kHz.

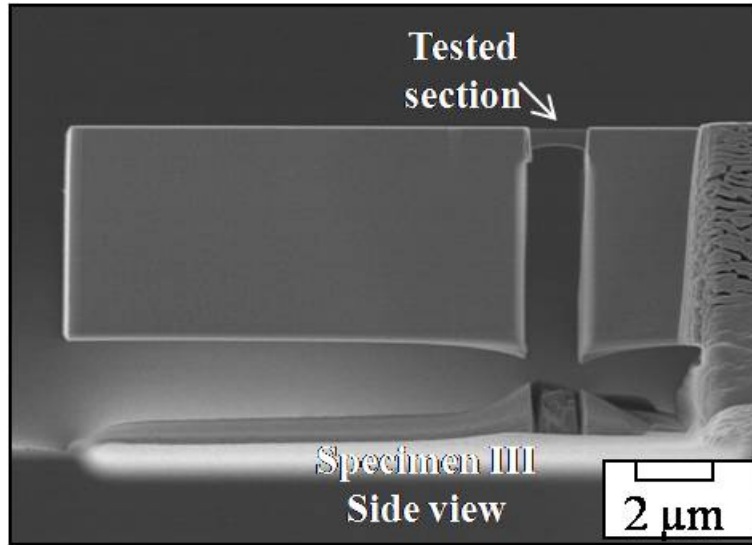


(a)

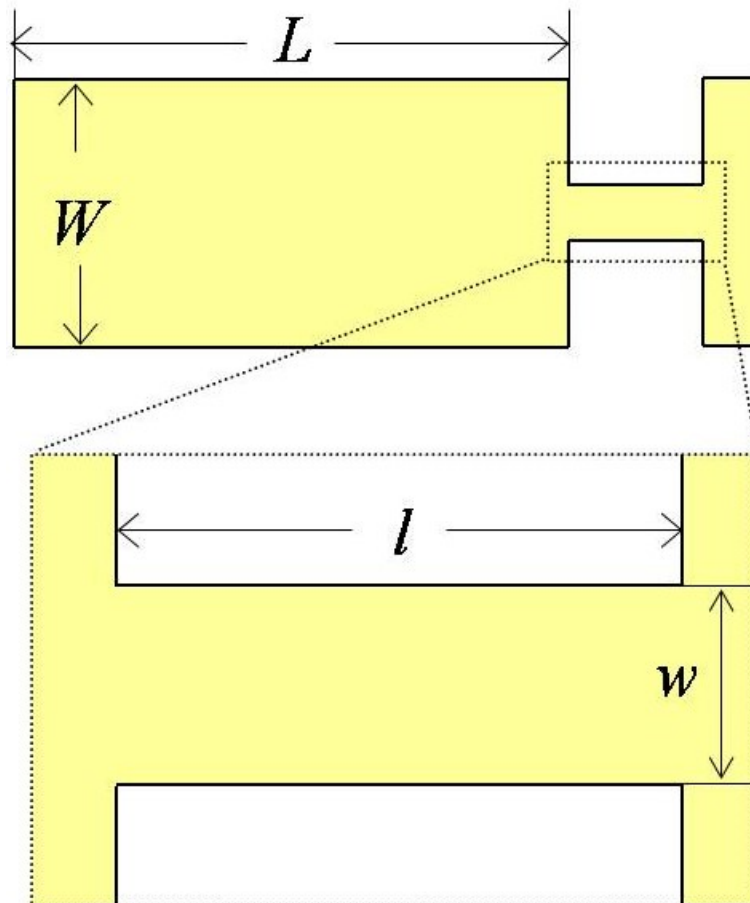


(b)

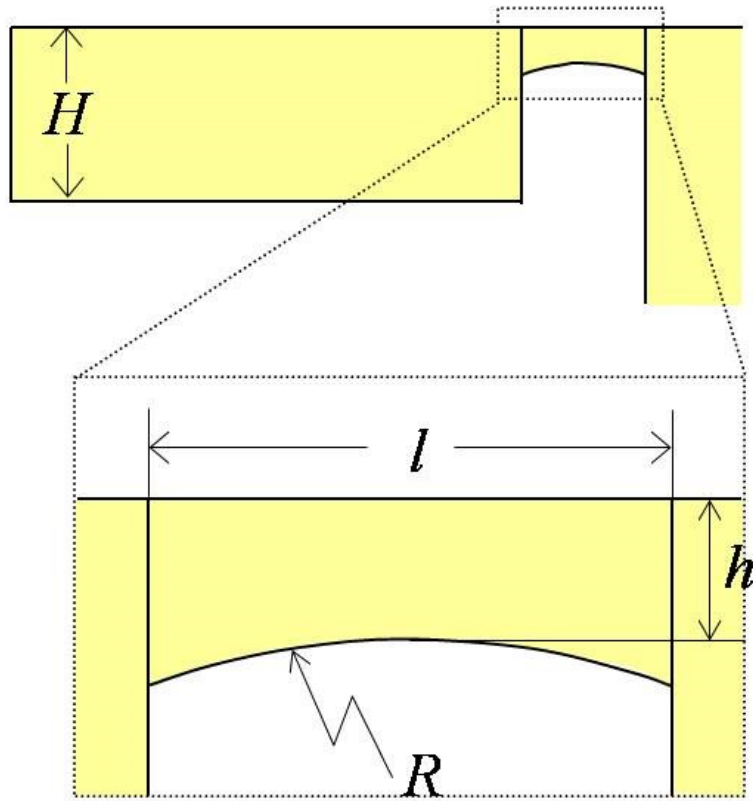




(c)



(d)



(e)

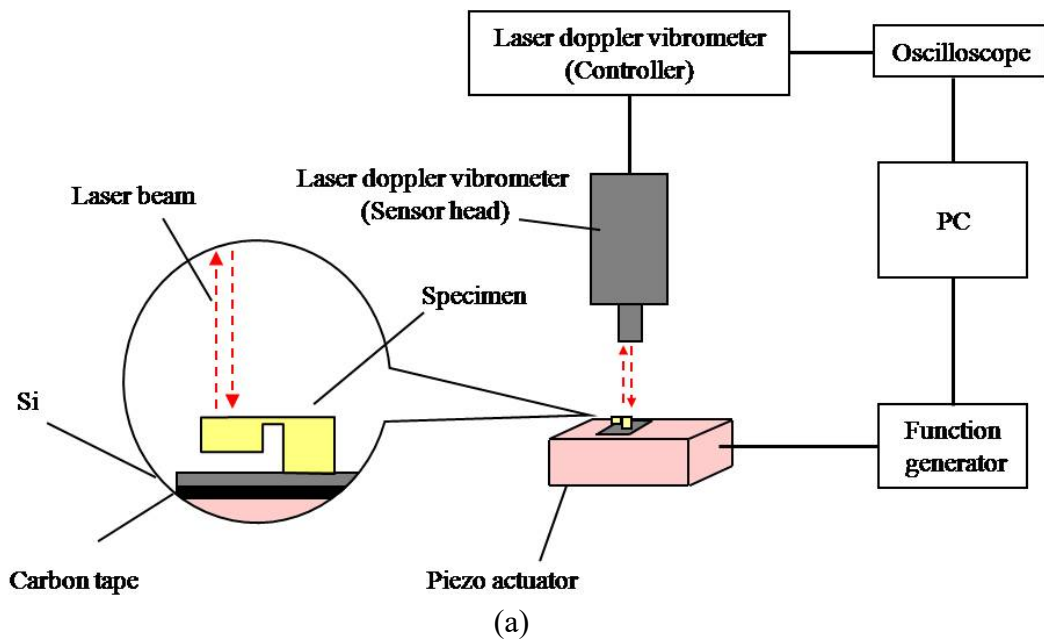
Fig. 4 FE-SEM images (top and side view): Specimen I (a), Specimen II (b), Specimen III (c), and schematic illustration of geometry of specimen: top view (d), side view (e)

Table 1. Specimen size (unit: nm)

| | w | h | l | R | W | H | L |
|--------------|------|------|-------|-------|-------|-------|-------|
| Specimen I | 5800 | 3964 | 14850 | 22500 | 30938 | 20840 | 60938 |
| Specimen II | 1280 | 810 | 3010 | 4500 | 15350 | 6440 | 20790 |
| Specimen III | 594 | 390 | 1388 | 2250 | 12470 | 5543 | 12352 |

2.2. Fatigue experiment

Figure 5 schematically illustrates the experimental system used in this work, which consists of a laminated piezoelectric actuator (Shoei system, PSt150/5×5/2), an operational amplifier (ELMOS, APA-10), a function generator (NF Corp., DF1906), a laser Doppler vibrometer (ONO SOKKI, LV-1720) and a control computer. The specimen is mounted on the piezoelectric actuator by cyanoacrylate adhesive. The function generator supplies a sinusoidal alternating voltage, which is magnified by the operational amplifier and sent to the actuator. The specimen is actuated in the vertical direction at room temperature in an air atmosphere. The displacement amplitudes at the weight top, $\Delta\delta_1/2$, and the test section root, $\Delta\delta_2/2$, are measured by means of the laser Doppler vibrometer. The net displacement width $\Delta\delta/2$ is given by the difference, $(\Delta\delta_1 - \Delta\delta_2)/2$ (Fig. 5b).



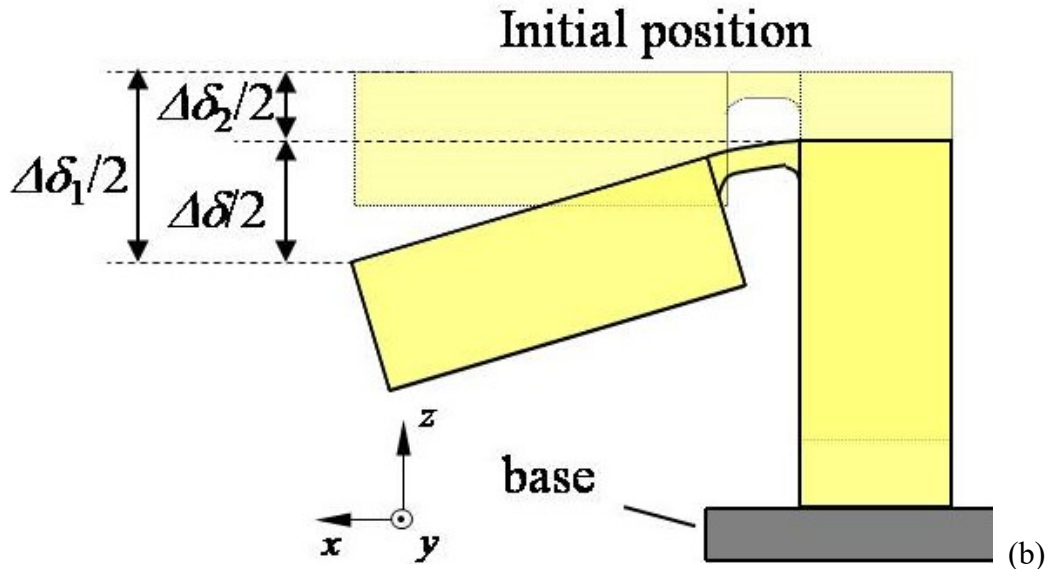


Fig. 5 Experimental system used in resonant fatigue experiment (a) and definition of displacement amplitude of specimen (b).

Before the fatigue experiment, the resonant frequency (f_0) of each specimen is preliminarily evaluated by vibration with a small displacement amplitude at frequencies between 0 and 100 kHz in intervals of 0.01 kHz.

The fatigue experiment is then carried out at the resonant frequency. After 10^7 cycles, the vibration is terminated and f_0 is measured with a small displacement amplitude. If fatigue damage appears in the specimen, the resonant frequency would shift. If there is no change in f_0 , the fatigue loading is applied with a higher amplitude. This process is repeated until a remarkable change in f_0 is observed. Resonant mode would be affected by localized damage too, so the change of the displacement amplitude $\Delta\delta_1/2$ is monitored during the fatigue as well.

Once the changes are observed, the surfaces of the test section are carefully examined by means of a field emission scanning electron microscope (FE-SEM)

to confirm the damage and its detail.

3. Analytical procedure

3.1 Vibration analysis

The resonant frequency and mode of each specimen is analyzed by a commercial code of finite element method (FEM) (ABAQUS (ver. 6.5-6)). The shape is reconstructed from the SEM images of each specimen, and the test section is divided into fine elements as shown in Fig. 6 (Specimen I). The elastic constants of an gold single crystal ($C_{11} = 192.44$ GPa, $C_{12} = 162.98$, and $C_{44} = 42.0$) are used in the simulation based on the crystal orientation of the specimen.

3.2 Stress analysis

Since elastic deformation is dominant in the high-cycle fatigue, the stress in the test section is analyzed by the elastic FEM (ABAQUS). The amplitude of vibration $\Delta\delta/2$, which is measured in the experiment, is applied to the end of the weight as static displacement.

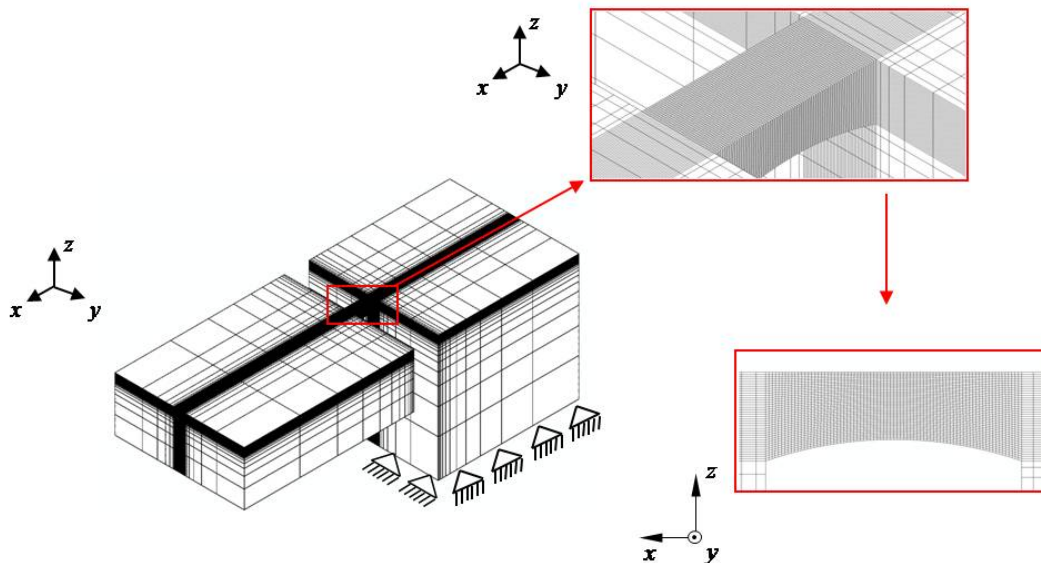


Fig. 6 Illustration of FEM mesh of the Specimen I

4. Experimental Results and Discussion

Specimen I

Before the fatigue experiment, f_0 and the vibration modes are evaluated by the FEM vibration analysis, and by vibration test with a small displacement amplitude. f_0 of the target bending mode (Fig. 5(b)) is 55.4 kHz.

$\Delta\delta_1/2$ is constant up to 10^7 cycles under the input voltage amplitudes of $\Delta V_{in}/2 = 0.3$ V ($\Delta\delta_1/2 \approx 1000$ nm), 3.0 V ($\Delta\delta_1/2 \approx 1200$ nm) and 5.0 V ($\Delta\delta_1/2 \approx 1500$ nm). However, the peak (f_0) shifts to 53.95 kHz after the fatigue under $\Delta V_{in}/2 = 5.0$ V from $f_0 = 55.4$ kHz before the fatigue.

Figure 7 shows the FE-SEM images of the gold surface before/after the fatigue test. While no damage exists before the experiment, extrusion/intrusion emerges on the cantilever surface after the fatigue loading of $\Delta V_{in}/2 = 5.0$ V. The total width of extrusions/intrusions is about 1 μm . The single extrusion or intrusion, which have the width of several-hundred-nanometers, is composed of many steps with the distinct traces. The traces have straight line-like appearance and are inclined at an angle of about 30 degrees to the tensile load applied (x -axis), i.e. the slip system B4. The distance between two adjacent traces is basically identical and about 10 nm. The threshold resolved shear stress on the B4 for extrusion/intrusion formation, identified by the FEM at $\Delta V_{in}/2 = 5.0$ V, $\Delta\tau_{trss}$, is 60 MPa.

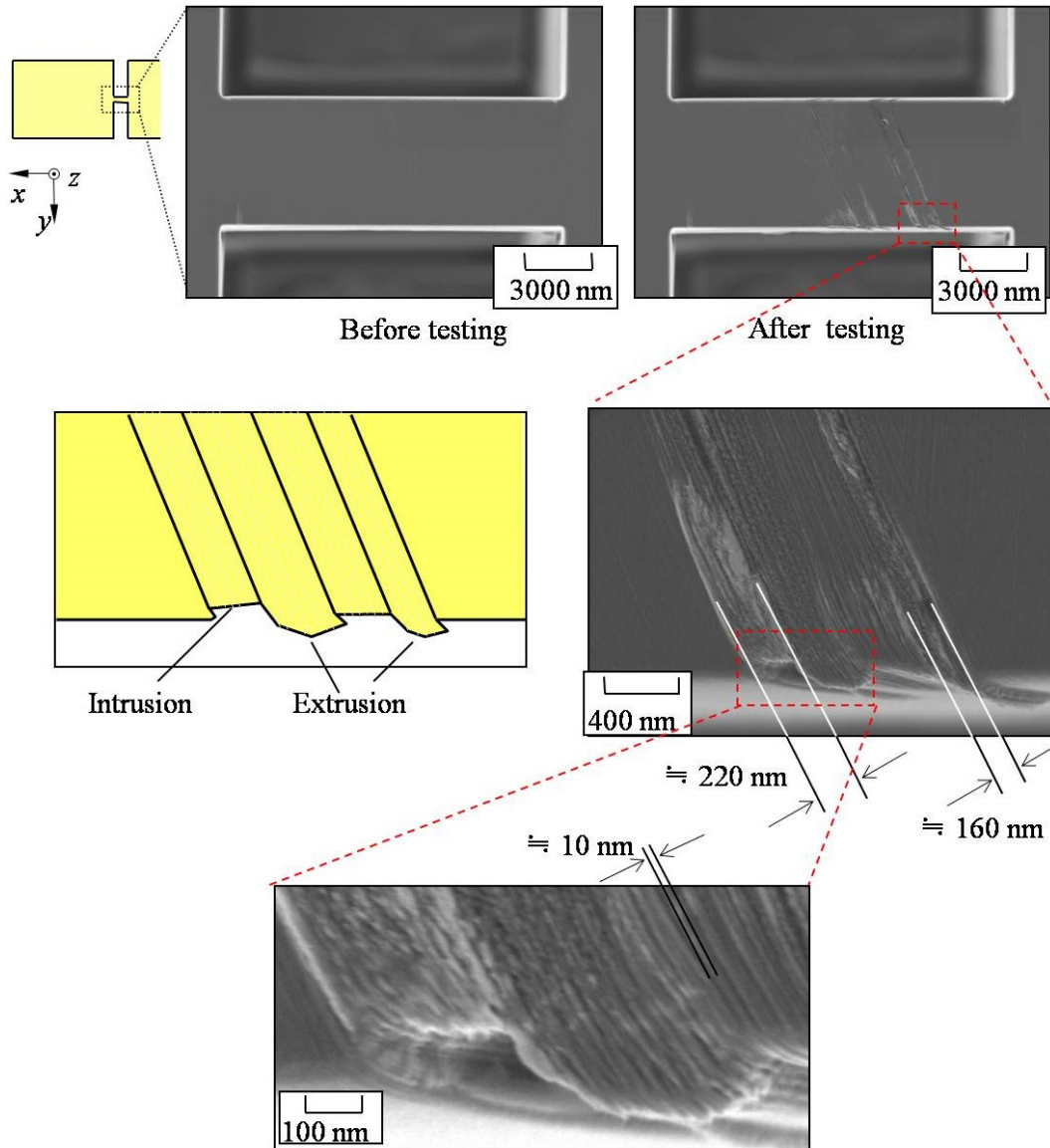


Fig. 7 FE-SEM images of the test section of Specimen I before/after the fatigue experiment with $\Delta V_{in}/2 = 5.0$ V: top view and the detail and illustration of slip bands formation

Specimen II

The resonant frequency before the fatigue is 72.9 kHz. With the input voltage amplitudes of $\Delta V_{in}/2 = 0.3$ V, 0.5 V and 1.0 V, f_0 is almost constant after 10^7 cycles and $\Delta\delta_1/2$ is constant up to 10^7 cycles. With $\Delta V_{in}/2 = 1.5$ V, $\Delta\delta_1/2$ goes

up to about 1100 nm and eminently decreases at about 1.4×10^5 cycles. The peak (f_0) shifts to 72.64 kHz after then.

Figure 8 shows FE-SEM images of the specimen surface before and after the fatigue test with $\Delta V_{in}/2 = 1.5$ V. The extrusion/intrusion emerges on the cantilever surface after the fatigue, which has the total width of about 200 nm. The width of single extrusion or intrusion is about one-hundred-nanometers, and it is composed of numerous distinct traces which have straight line-like appearance and are parallel to the slip system B4. The distance between two adjacent traces is basically identical and about 10 nm. The threshold resolved shear stress on the B4 for extrusion/intrusion, $\Delta\tau_{trss}$, is 113 MPa.

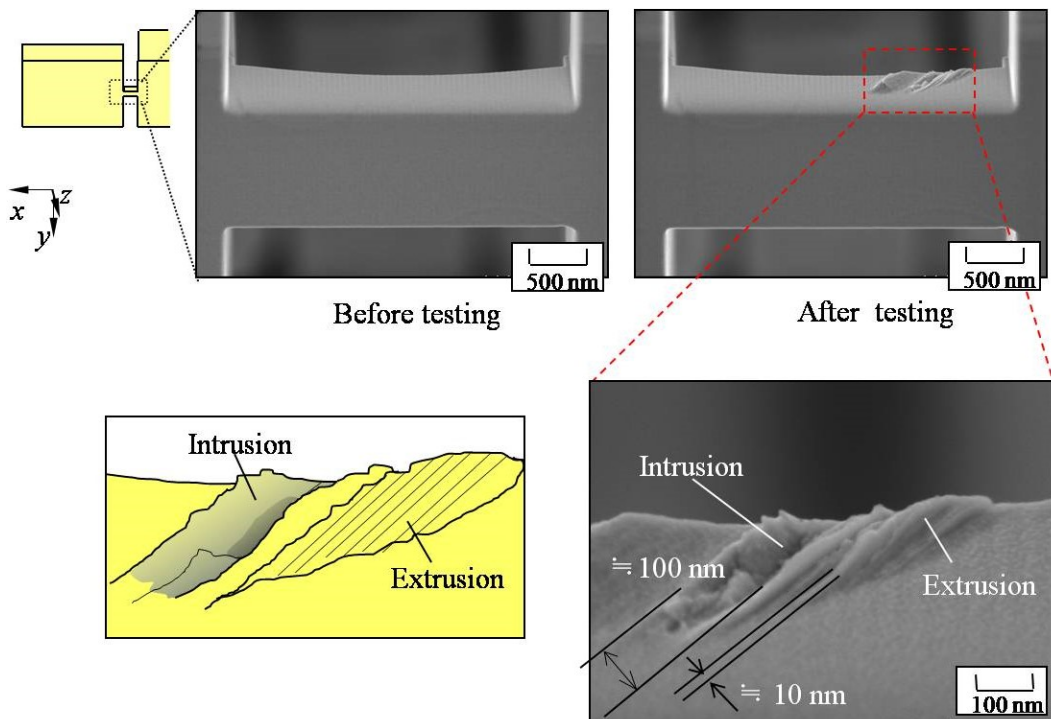


Fig. 8 FE-SEM images of the test section of Specimen II before/after the fatigue experiment with $\Delta V_{in}/2 = 5.0$ V: tilt view (-25°) and the detail and illustration of slip bands formation

Specimen III

The resonant frequency before the fatigue experiment is 58 kHz. With input voltage amplitudes of $\Delta V_{\text{in}}/2 = 1.5$ V, $\Delta\delta_1/2$ is constant up to 10^7 cycles and f_0 is constant after 10^7 cycles. With $\Delta V_{\text{in}}/2 = 2.5$ V, $\Delta\delta_1/2$ goes up to about 1300 nm and eminently decreases at about 1.2×10^6 cycles. The peak (f_0) shifts to 57.9 kHz at $\Delta V_{\text{in}}/2 = 2.5$ V.

Figure 9 shows FE-SEM images of the gold surface before and after the fatigue test with $\Delta V_{\text{in}}/2 = 2.5$ V. The observed traces have a straight line-like appearance and are parallel to the B4 slip system. The extrusion/intrusion has the width of about 20 nm composed of two slip traces, and the distance between two traces is about 10 nm. The threshold resolved shear stress on the B4 for extrusion/intrusion, $\Delta\tau_{\text{trss}}$, is 246 MPa.

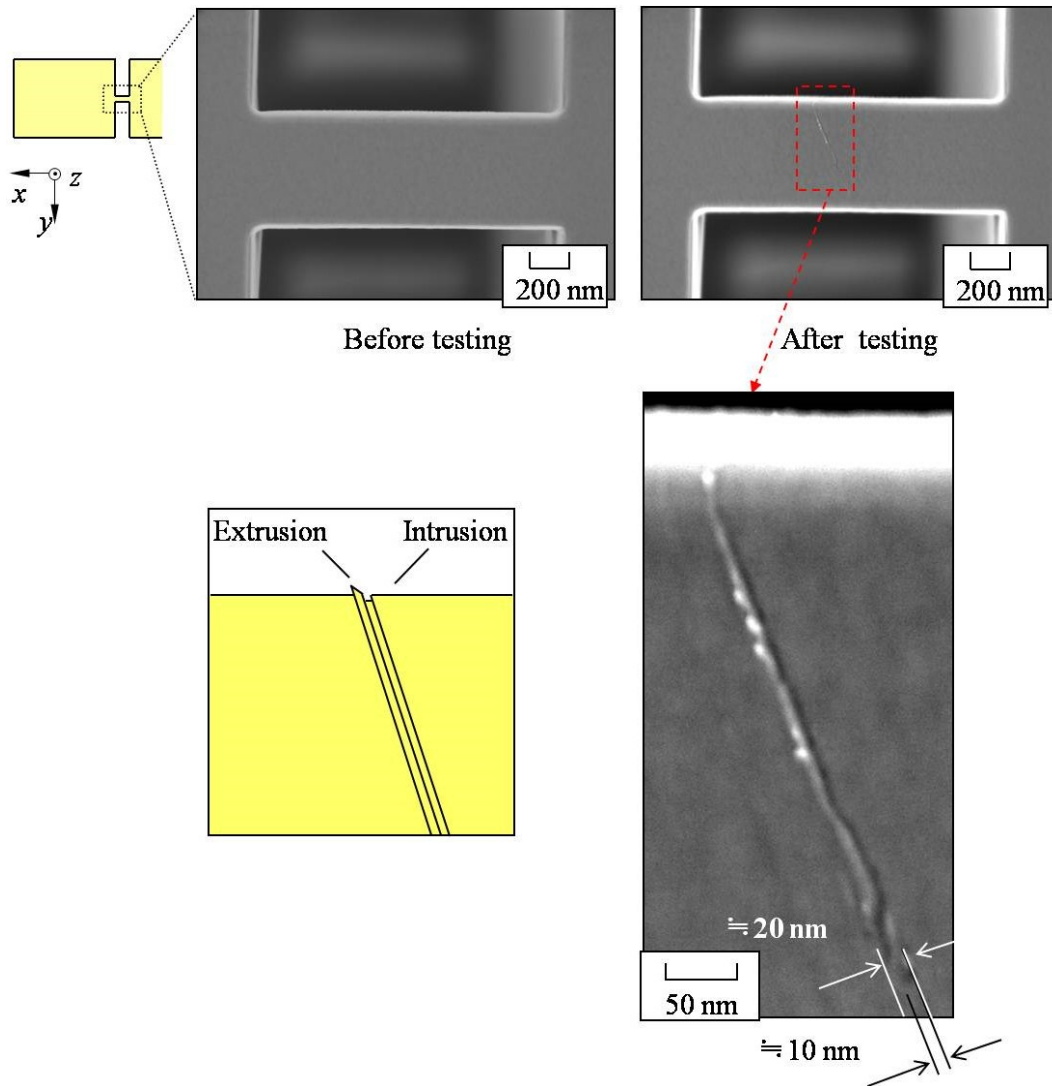


Fig. 9 FE-SEM images of the test section of Specimen III before/after the fatigue experiment with $\Delta V_{in/2} = 5.0$ V: top view and the detail and illustration of slip bands formation

Size - Dependence

In fatigue of a Fcc bulk metal at low and intermediate amplitudes, persistent slip band (PSB) with lamellar structure is formed along the crystallographic plane with the maximum resolved shear stress. The PSB includes self-organized understructures of dislocations such as ladder structure. The width of PSB is

usually thicker than a few micron and independent of the specimen size. The extrusion/intrusion, which brings about the crack initiation in fatigue, is formed at the intersection between the PSB and the specimen surface.

In this fatigue experiment, though the morphology of extrusion/intrusion is similar to the one in a bulk, the detail is different. The width is thinner for smaller specimen as shown in Fig. 10. The width of hundreds to tens nanometer is far finer than the ones in bulk. The high magnification images by the FE-SEM present that the extrusion/intrusion is composed of the traces, which are slip lines generated by dislocations on the slip system B4.

Figure 11 shows the relationship between specimen size h and threshold resolved shear stress $\Delta\tau_{trss}$. $\Delta\tau_{trss}$ are much higher than that of the PSB in bulk Au (23.4 MPa). Moreover, $\Delta\tau_{trss}$ is strongly dependent on the specimen size, while that of bulk single crystal is independent of it. It was repeated that uniaxial compression tests conducted on a single-crystal indicated a specimen size effect on the yield stress: gold pillar specimens with the diameters of 300 ~ 7450 nm. The flow stress rapidly increases as the diameter is reduced. One suggested interpretation of the results is that the dislocations leave through the surface; "dislocation starvation". This mechanism can explain high resolved shear stress of small-volume specimens. In the other words, there are not enough active dislocations to accommodate the imposed deformation.

When the resolved shear stress is high enough, the dislocation sources could be formed and slip lines are generated. FE-SEM analysis indicates that the slip lines formation is spatially periodic and the distance between adjacent ones is about 10nm in all specimens. In macroscale components, the dislocation sources

can be generated consecutively in the bulk of crystal due to double cross slip (DCS) type nucleation process which bring out slip lines, and the threshold ejection distance of DCS introduces spatially periodicity, which depends on the state of the crystal and stress field. In contrast, the consecutive sources activation by DCS in the bulk of small-volume specimens is very difficult once the dislocation-starved conditions are reached. Then, one of the possible assumptions concerning dislocation sources in this experiment is that nucleating form surface. The spatially periodicity of slip lines indicates the nucleated sources distribute evenly. However, more experimental data and theoretical calculations need been taken to determine in more detail the character of the spatially periodic behavior.

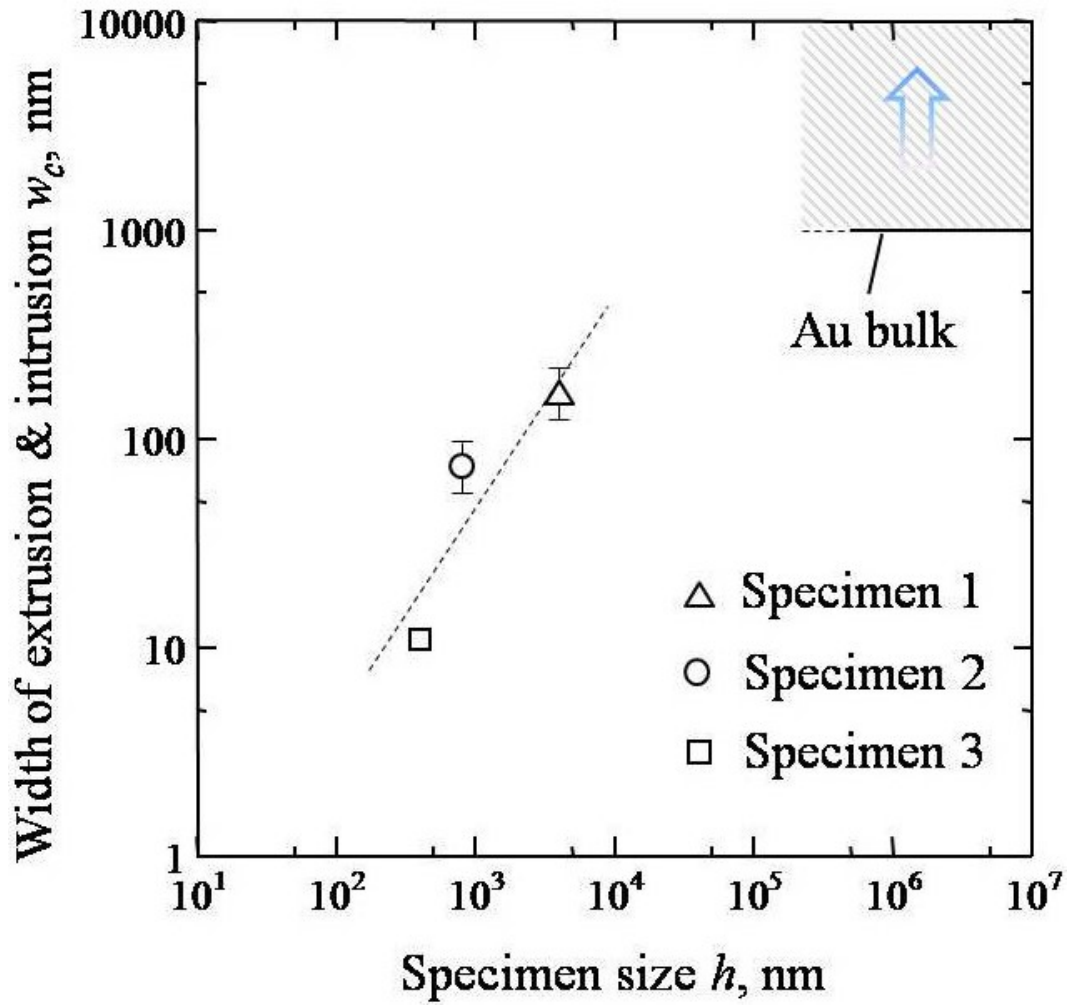


Fig. 10 Relationship between specimen size h and width of extrusion and intrusion w_c

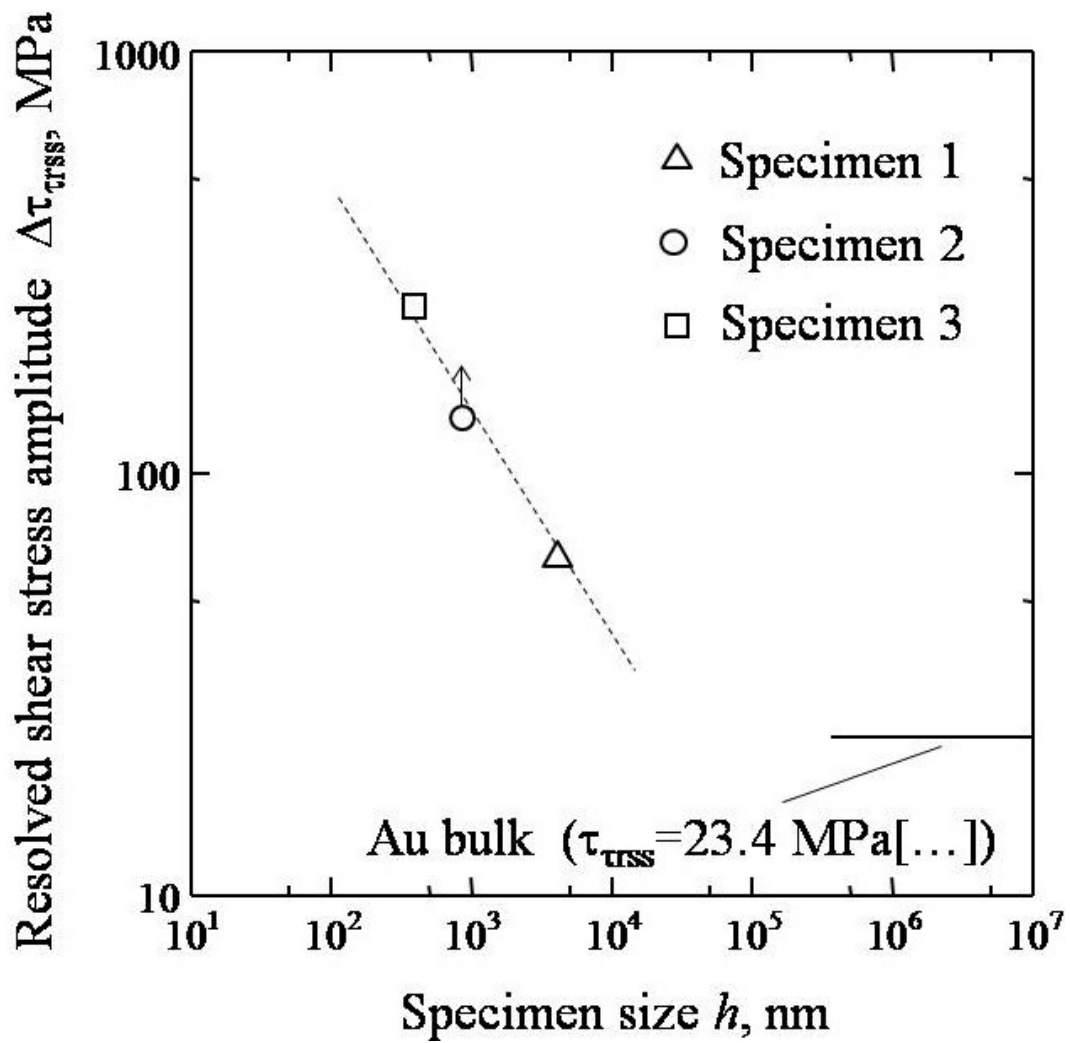


Fig. 11 Relationship between specimen size h and threshold resolved shear

stress $\Delta\tau_{crss}$

Chapetr 4: Formation of slip bands in nano-polycrystalline copper under high-cycle fatigue of SiTiCuSiN nanoscale material

2. Experimental procedure

2.1 Material and specimen

After the native oxidized layer on a single crystalline silicon (Si) (100) substrate is removed by argon ion etching, layers of titanium (Ti) (thickness: 20 nm), copper (Cu) (thickness: 200 nm), and silicon nitride (SiN (Si_3N_4)) (thickness: 20 nm) are continuously deposited by magnetron sputtering. While the Cu and SiN layers are polycrystal, the Si_3N_4 layer is amorphous. The multi-layered plate is annealed in vacuum (1×10^{-4} Pa) at 673 K for 1 h.

Figure 1 schematically illustrates the specimen in the method used for the resonant fatigue experiments. The specimen consists of a weight, a test section and a base. The test section is composed of the Si, Cu, Ti and SiN layers. The specimen is formed from the multi-layered plate using a focused ion beam (FIB) processing system (Hitachi, FB-2200) with accelerating voltage of 40 kV wherein the beam current is set to 1.17 nA.

The fabrication procedure used for the specimen is as follows.

1. A block of $25 \mu\text{m} \times 25 \mu\text{m} \times 25 \mu\text{m}$ dimensions is carved out of the multi-layered material (Fig. 2 (a)).
2. The block is cut from the substrate after a microprobe is attached to the upper surface by tungsten (W) deposition (Figs. 2 (b) and (c)).
3. The block is placed on a $5 \text{ mm} \times 5 \text{ mm}$ Si substrate (thickness $550 \mu\text{m}$) (Fig. 2 (d)) and is mounted by W deposition (Fig. 2 (e)). The microprobe is separated by FIB.
4. Similarly, a block for weight is carved out of an Au plate and is picked up by a microprobe. The Au block is mounted on the SiN layer of the multi-layered

- block, which was mounted on the Si substrate, by W deposition (Figs. 2 (f) and (g)).
5. A test section that includes the Si substrate and layers of Ti, Cu and SiN is fabricated using y - and z - direction beams with low currents of 0.02 nA (Fig. 2 (h)). The upper surface of the test section is flattened by a weak x -direction beam in order to avoid any difference in level at the interfaces (Fig. 2 (i)).
 6. In order to remove damaged and re-deposited layers introduced by FIB, argon (Ar) ion milling (HITACHI, Gentle mill-Hi; accelerating voltage: 0.3 kV, current: 8 μ A, processing time: 5 min) is performed on the surfaces of the test section.

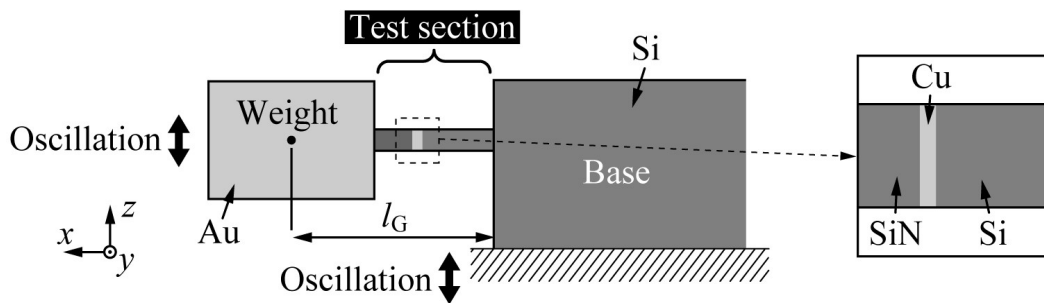


Fig. 1 Schematic illustration of the resonant fatigue experimental method. A specimen consists of a weight, a test section and a base.

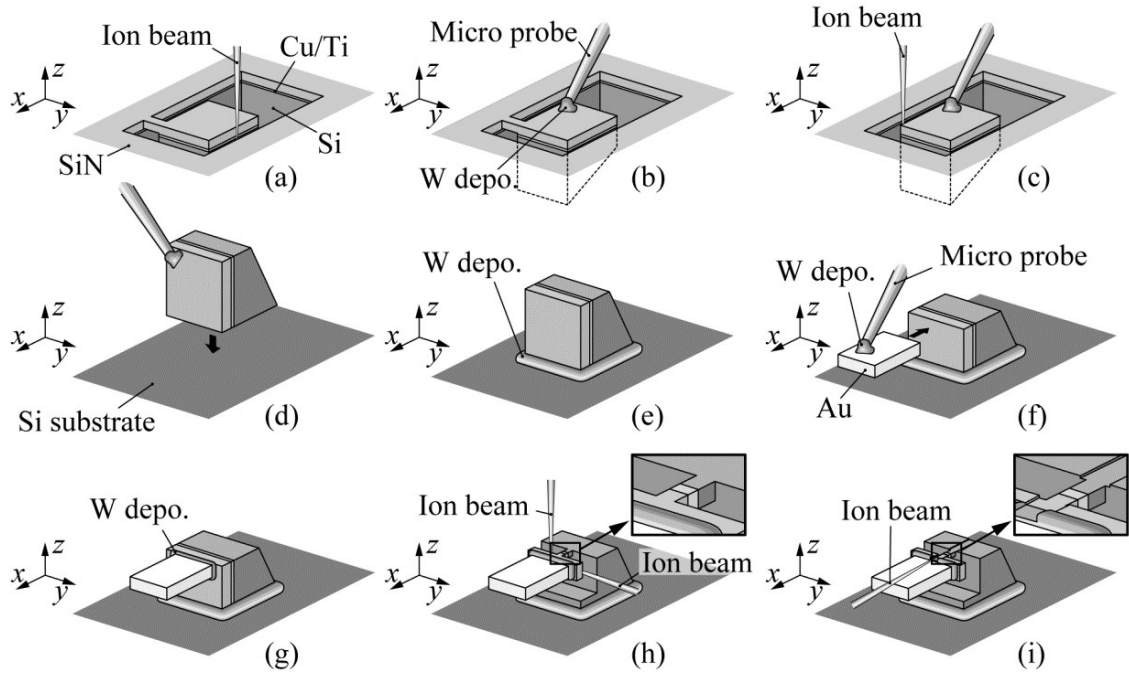


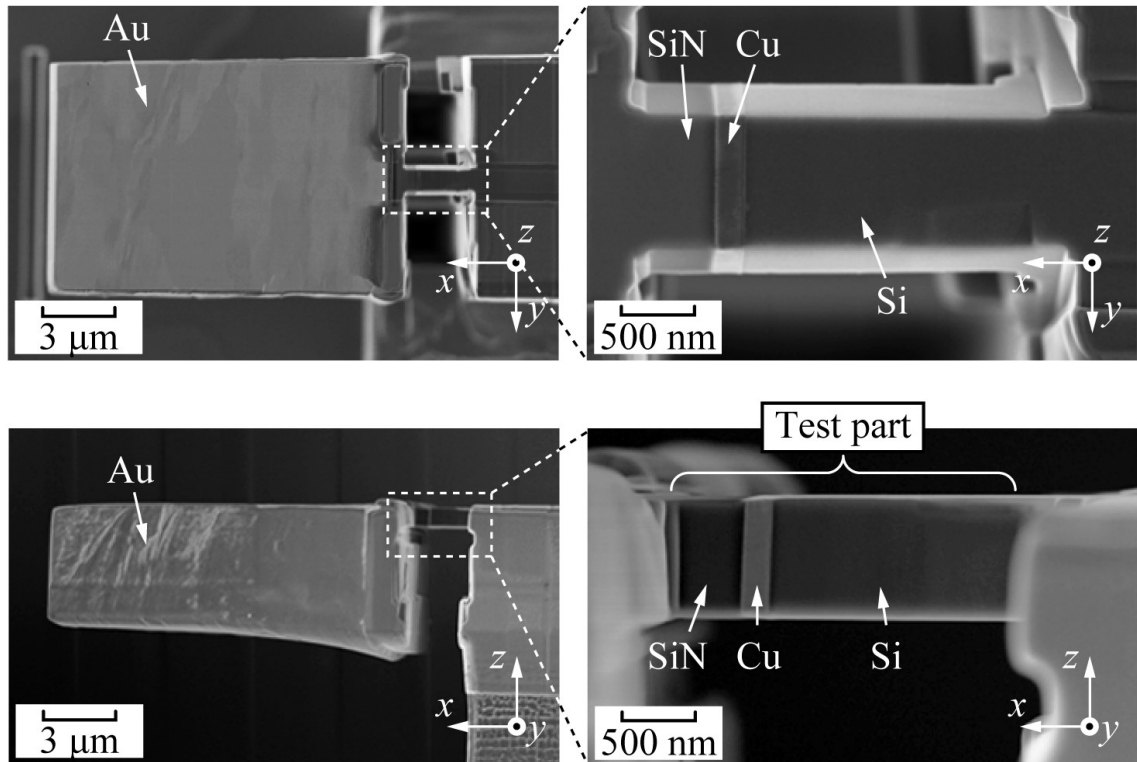
Fig. 2 Schematic illustration of the specimen preparation method using FIB.

By inducing oscillation in the vertical direction to the base, as shown in Fig. 1, a fully-reversed bending load is applied to the test section. The resonant frequency of the nano-/micro-scale material is usually more than a few tens of GHz. However, too high a resonant frequency brings about difficulties in control of the fatigue cycle because a number of 10^7 cycles, commonly defined as the number of cycles of the fatigue limit, is attained in less than 1 second. This can be reduced by removing the weight attached to the cantilever tip. The resonance frequency, f_0 , of a cantilever (cross-section of w (width) \times h (height)) with a heavy weight at the end is approximately evaluated by the following equation.

$$f_0 = \frac{1}{2\pi} \sqrt{\frac{k}{m}} \quad \left(k = \frac{Ewh^3}{4l_G^3} \right) \quad (1)$$

Here, k is the spring constant of the test section in the vibration direction, m is the mass of the weight, E is the Young's modulus of the test section and l_G is the length from the test section root to the gravity center of weight. Based on Eq. (1), the shape and size of the weight are adjusted so that $f_0 < 300$ kHz is achieved.

Figure 3 shows (a) scanning electron microscope (SEM) images of the fabricated specimen and (b) the specimen size. In the test section, the surface is flat and there are no steps or defects. Only Cu shows preferential plastic deformation because of the lowest yield stress in the constituent materials.



(a)

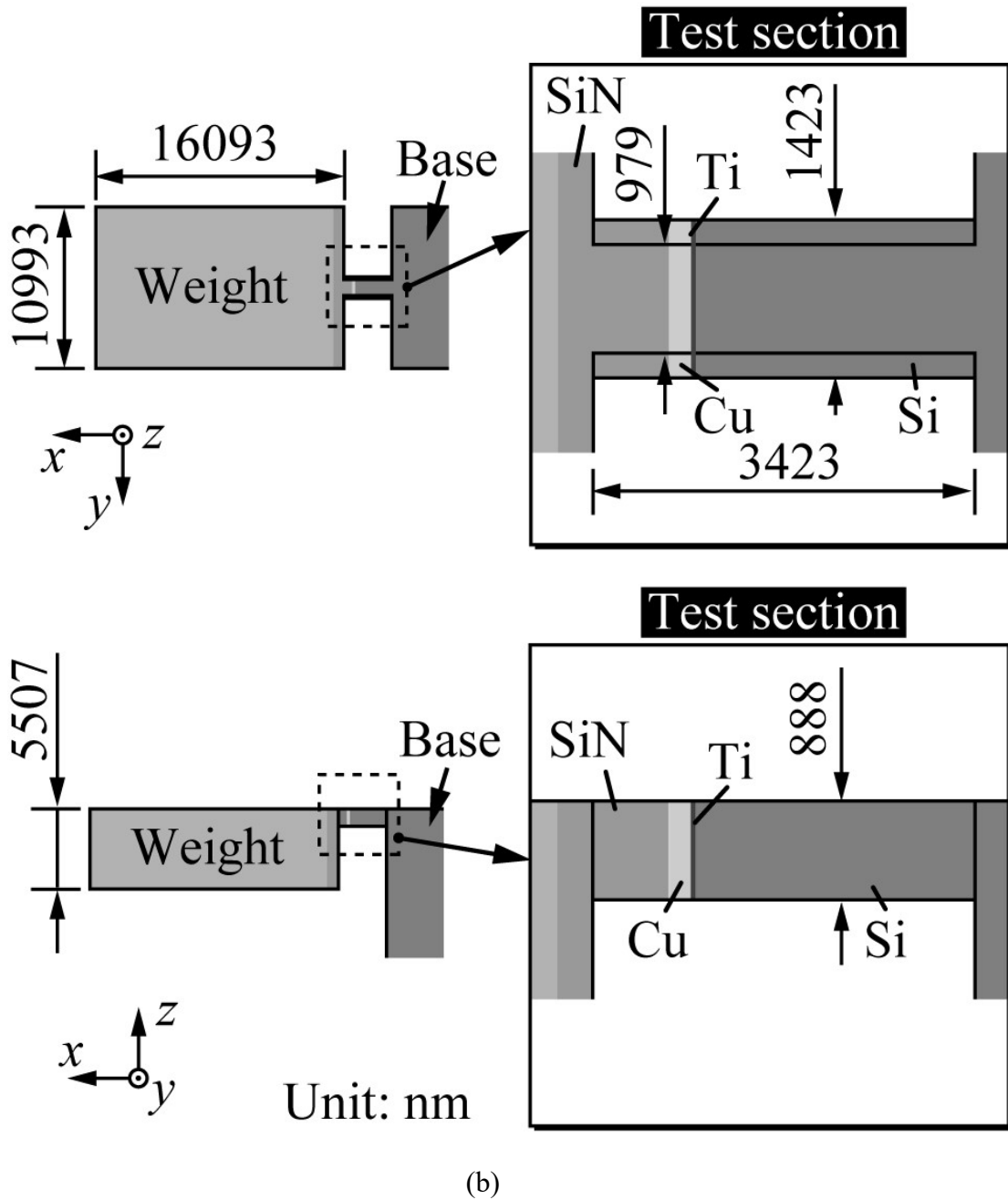


Fig. 3 Specimens fabricated by FIB. (a) SEM images and (b) dimensions of the specimen.

If bending deformation in the vertical direction is applied to the test section with a rectangular cross-section, the maximum stress appears on both the upper and lower surfaces. In the experiment, in order to restrict fatigue damage on the

upper surface, a trapezoidal cross-section is adopted for the cantilever. The ratio of normal stress in the longitudinal direction on the upper surface, σ_u , to that on the lower surface, σ_b , is given by the following equation.

$$\frac{\sigma_u}{\sigma_b} = \frac{2 + w_u/w_b}{1 + 2w_u/w_b} \quad (2)$$

Here, w_u and w_b are the lengths of the upper and bottom bases of the trapezoid cross-section, respectively. We set w_u/w_b to 3/4 so that stress on the upper surface is about ten percent higher than that on the lower surface.

The crystallographic information on the upper surface of the Cu portion in the test section is analyzed by electron backscatter diffraction (EBSD). Figure 4(a) shows the shape and crystal orientation of grains obtained by EBSD. The color in the map corresponds to that in a standard stereo-triangle shown in the figure and indicates the crystallographic orientation to the y -axis. Although each grain is identified, uncertain (black) domains exist near the boundaries between grains owing to the resolution of the EBSD. Thirteen coarse grains are observed in the Cu portion, numbered 1-13 in Fig. 4(b). Figure 4(c) shows the stereographic projections of these 13 grains. In the stereograph, the slip plane and slip direction determined by the loading direction and crystalline orientation are denoted as A-D and 1-6, respectively, in accordance with the Schmid and Boas notations. The slip system with the highest Schmid factor (primary slip system) is expressed as B4.

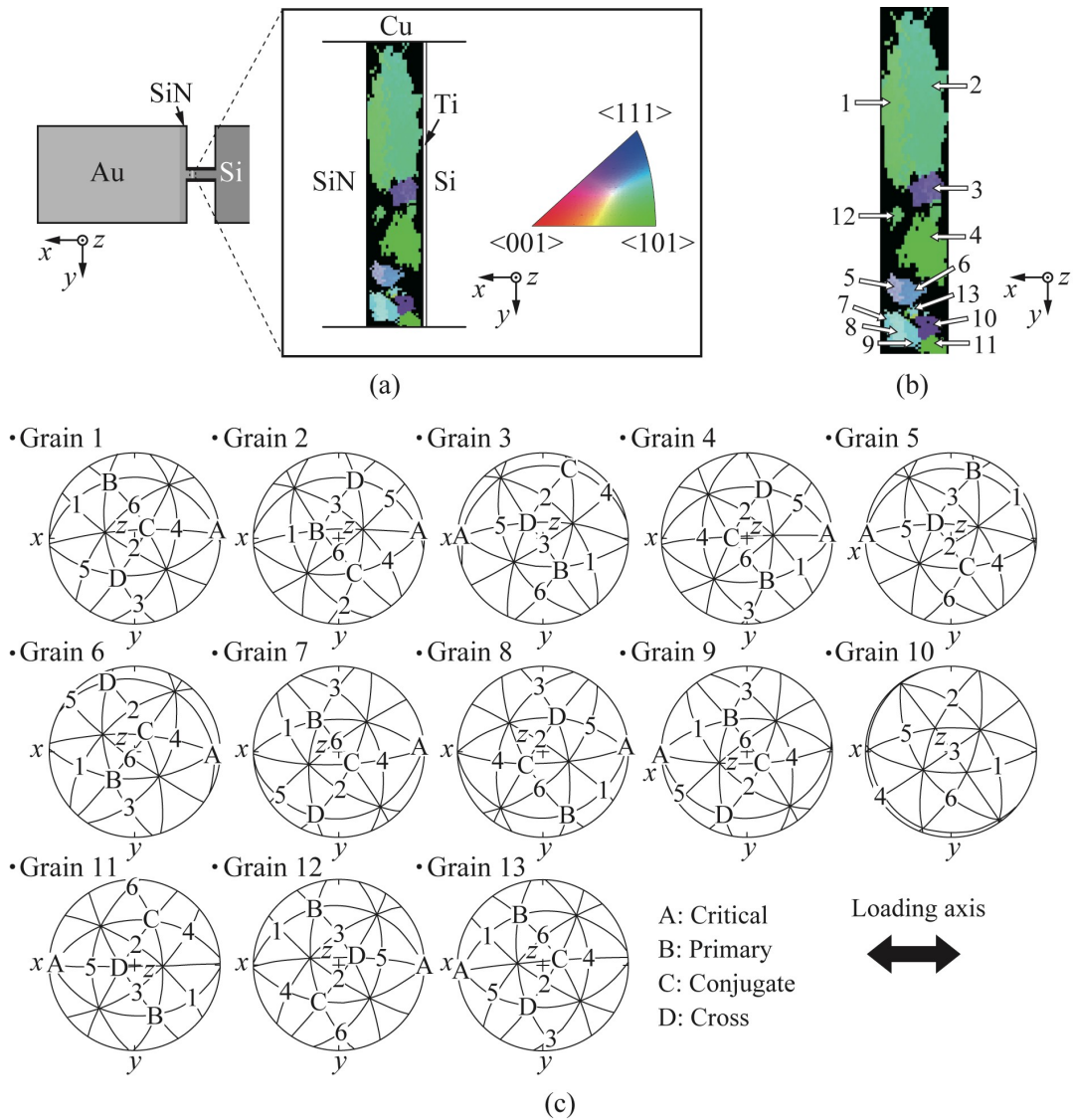


Fig. 4 Crystallographic orientation in Cu. (a) Inverse pole figure map showing the orientation of individual grains on the upper surface of the Cu portion in the test section, (b) locations of the individual grains indicated by numbers, and (c) stereographic projections of Grains 1-13.

2.2 Fatigue experiment

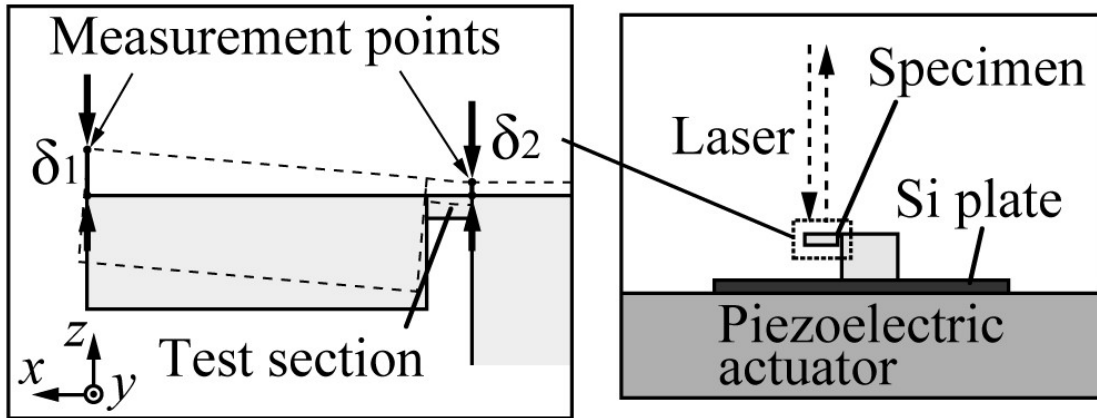
Figure 5 schematically illustrates the experimental system used in this work, consisting of a laminated piezoelectric actuator (Shoei system, PSt150/5×5/2), an operational amplifier (ELMOS, APA-10), a function generator (NF Corp.,

DF1906), a laser Doppler vibrometer (ONO SOKKI, LV-1720) and a control computer.

The Si plate with the specimen is mounted on the top face of the piezoelectric actuator using a cyanoacrylate adhesive. The function generator supplies a sinusoidal alternating voltage with a constant amplitude, which is amplified by the operational amplifier and sent to the actuator. The specimen is oscillated in the vertical direction at room temperature in an air atmosphere. The displacement amplitude at the weight top, $\Delta\delta_1$, and the test section root, $\Delta\delta_2$, are measured by means of the laser Doppler vibrometer. The laser beam is narrowed down to about 10 μm using a 20-power objective lens.

Before the fatigue experiment, the resonant frequency of the specimen is preliminarily evaluated by oscillation at frequencies between 0 and 200 kHz in intervals of 0.15 kHz with a small displacement amplitude. A resonance fatigue experiment is then carried out at the resonant frequency. In the resonant fatigue experiment, when fatigue damage appears in the test section, the displacement range sharply decreases owing to the change in f_0 .

After 10^7 cycles, the oscillation is terminated and f_0 is measured with a small displacement amplitude. If there is no change in $\Delta\delta_1$ and f_0 , oscillation is applied with an amplitude that is about 0.3V-0.7 V higher than the previous one. This is repeated until a remarkable change in $\Delta\delta_1$ and f_0 is observed. After the fatigue experiment, the surfaces of the test section are carefully observed by means of a field emission scanning electron microscope (FE-SEM).



Laser Doppler vibrometer

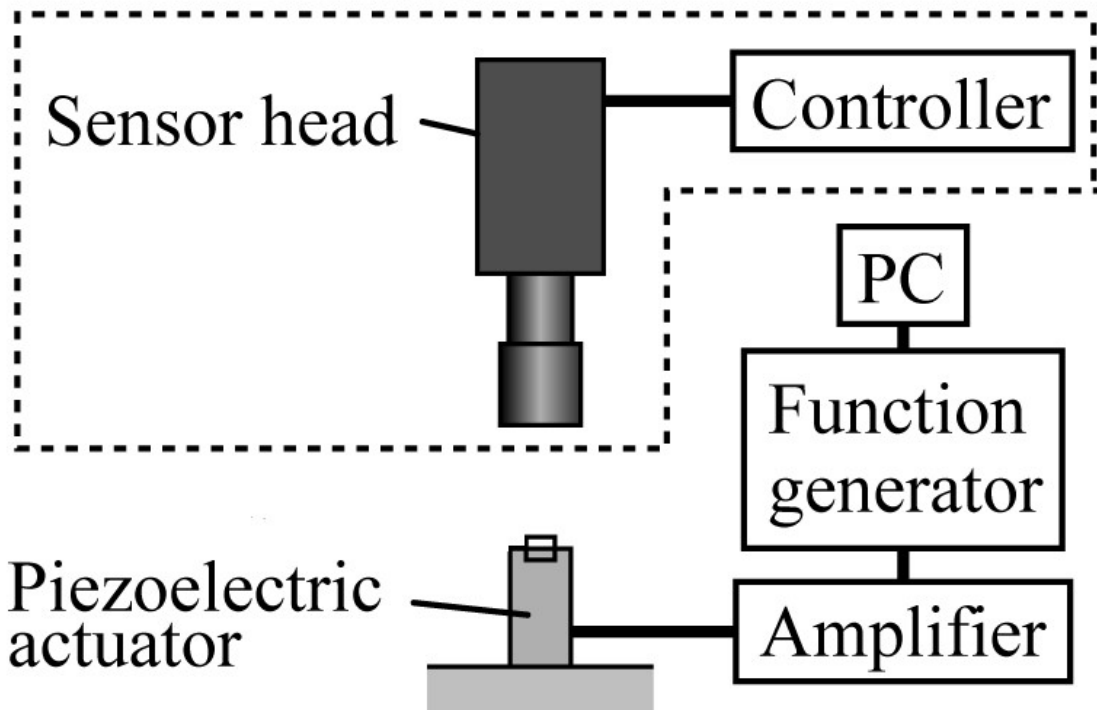


Fig. 5 Experimental system used for the resonant fatigue experiments.

3. Analytical procedure

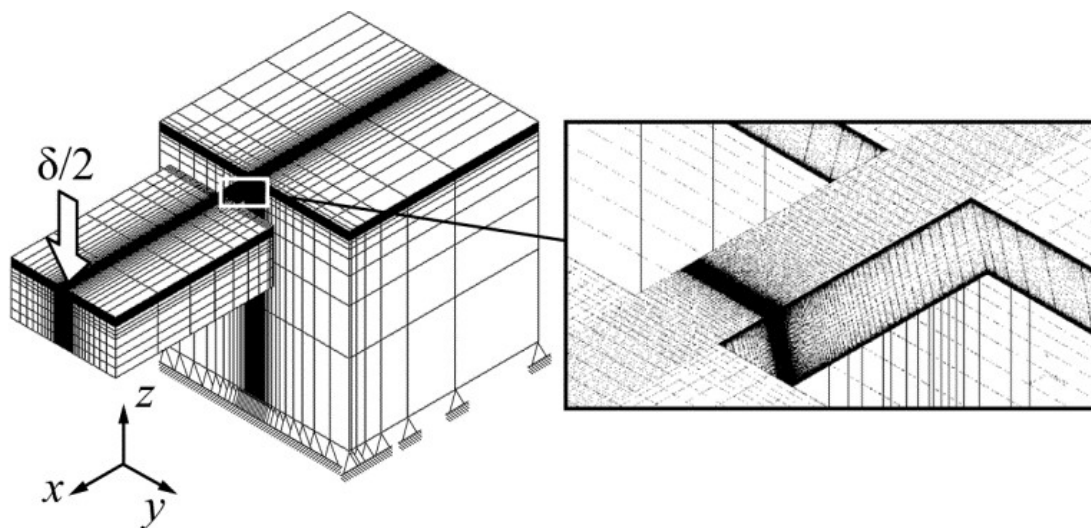
3.1 Oscillation analysis

The vibration mode and f_0 of the specimen is analyzed by the finite element method (FEM). Figure 6 shows (a) the mesh division of the analytical model and (b) constants of the constituent materials. The shape is reconstructed from the

SEM images of the specimen. The region near the dissimilar interfaces, where stress concentration is expected, is divided into fine meshes (minimum element size: 1.8 nm). Although orthotropic anisotropy is considered in the Si single crystal substrate, other materials (Ti, Cu, SiN) are treated as a homogeneous substance. A perfect constraint condition is imposed at the bottom end of the model.

3.2 Stress analysis

The stress in the test section is analyzed by elastic FEM using the model shown in Fig. 6. The static displacement amplitude $\Delta\delta/2$ ($\Delta\delta$: net displacement width ($= \Delta\delta_1 - \Delta\delta_2$)), which is observed in the experiment, is applied to the end of the weight (measurement position of δ_1) as shown in Fig. 6. A commercial analytical code (ABAQUS (ver. 6.5-6)) is used for the vibration and stress analyses.



(a)

| Material | E [GPa] | d [g/cm ³] | ν |
|----------|-----------|--------------------------|-------|
| Cu | 129 | 8.82 | 0.334 |
| SiN | 200 | 3.44 | 0.27 |
| Ti | 115.7 | 4.51 | 0.32 |
| Au | 78 | 19.3 | 0.44 |

| Material | C_{11} [GPa] | C_{12} [GPa] | C_{44} [GPa] | d , g/cm ³ |
|----------|-------------------|-------------------|-------------------|-------------------------|
| Si | 167.4 | 65.23 | 79.57 | 2.33 |

(b)

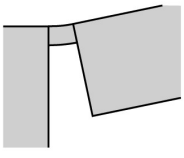
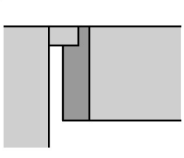
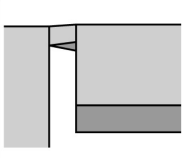
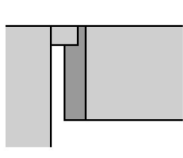
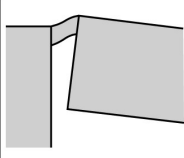
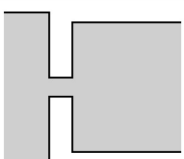
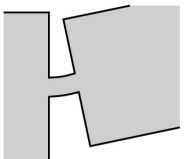
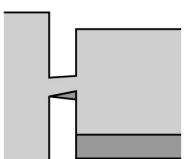
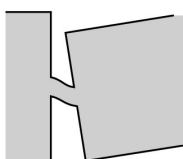
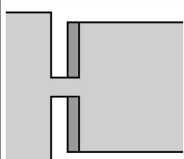
Fig. 6 (a) FEM mesh of the specimen, and (b) material constants of the constituent materials.

4. Results and discussion

4.1 Resonant frequency and Stress distribution

The values of f_0 for the oscillation modes (Mode 1 - Mode 5) obtained from the oscillation FEM analysis are listed in Table 1. The f_0 of Mode 1, which is the target oscillation mode here, is 150.24 kHz. Other modes are not intermingled because their f_0 values are separated from that of Mode 1 in the magnitude of more than 50 kHz. Figure 7 shows the frequency response curve at the specimen end obtained by oscillation with a low displacement amplitude before the fatigue experiment. A prominent peak exists at $f_0 = 149.39$ kHz, which is close to the f_0 of Mode 1 obtained by the vibration analysis. This indicates that the specimen resonates only in Mode 1.

Table 1 Resonant frequencies in the five oscillation modes of the specimen.

| | Mode 1 | Mode 2 | Mode 3 | Mode 4 | Mode 5 |
|-----------------------|---|---|--|---|---|
| f_0 | 150.24 kHz | 200.86 kHz | 552.12 kHz | 3040.56 kHz | 4292.93 kHz |
| Side view of specimen |  |  |  |  |  |
| Top view of specimen |  |  |  |  |  |

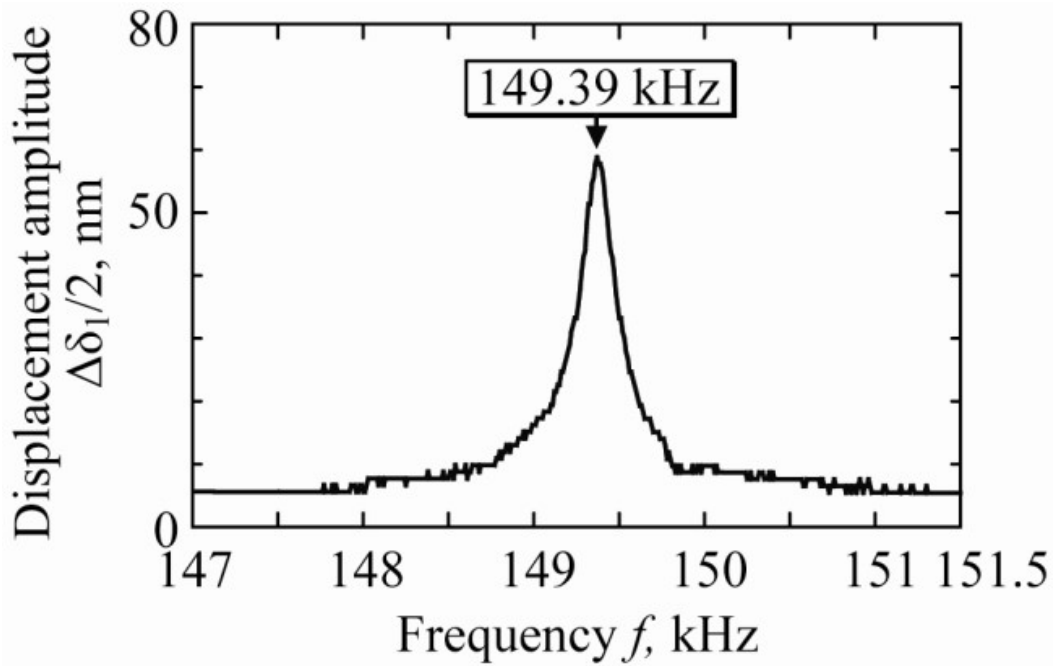


Fig. 7 Frequency response curve of the displacement amplitude at the root of the specimen obtained before the resonant fatigue experiment.

Figure 8 shows the distribution of the absolute value of the normal stress in the x -direction, $|\sigma_x|$, on the upper surface and on the Ti/Cu interface on the Cu

side. The distribution is obtained by the stress FEM analysis where a downward displacement of $\delta/2 = 1000$ nm is applied to the measurement position of δ_1 (see Fig. 6). The neutral plane of bending deformation is located near the lower surface because of the trapezoidal shape in the cross-sectional geometry. The stress on the upper surface is about ten percent higher than that on the lower surface, and the level near the Ti/Cu interface is higher than that near the Cu/SiN interface.

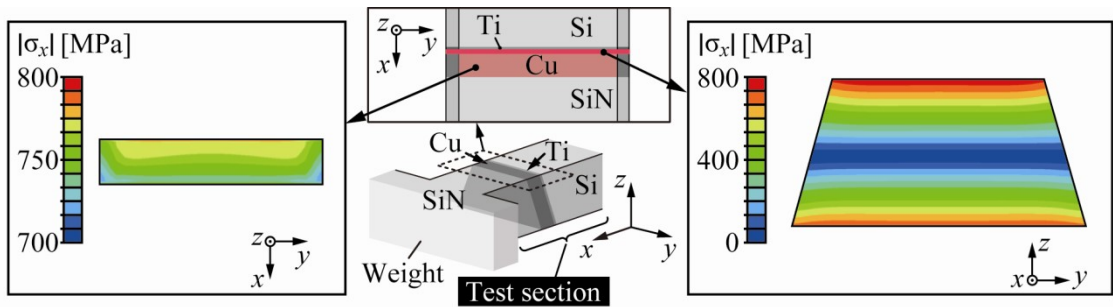
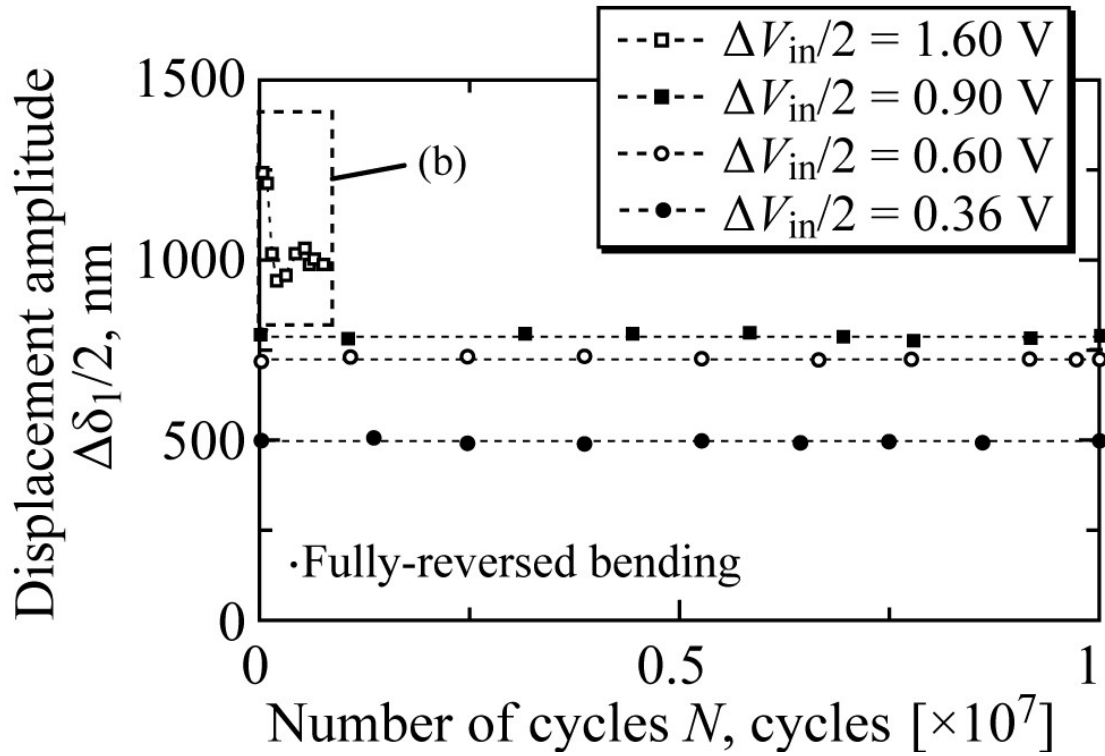


Fig. 8 Distribution of the absolute value of σ_x when a load with a downward displacement of $\delta/2 = 1000$ nm is applied to the observation position of δ_1 .

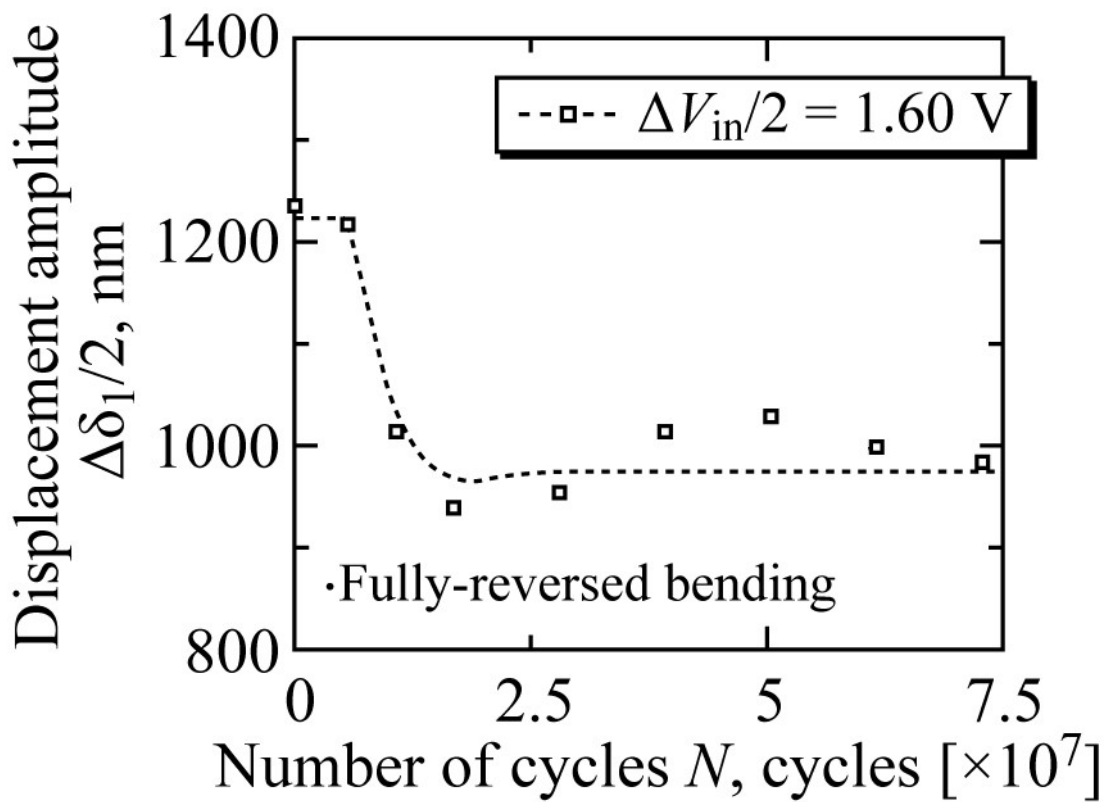
4.2 Resonant Fatigue

Figure 9(a) shows the relationship between the displacement amplitude at the specimen end $\Delta\delta_1/2$ and the number of cycles N . At $\Delta V_{in}/2 \leq 0.90$ V, $\Delta\delta/2$ increases with increasing $\Delta V_{in}/2$ and is constant up to 10^7 cycles. Although $\Delta\delta/2$ goes up to about 1200 nm at $\Delta V_{in}/2 = 1.60$ V, it eminently decreases when the number of cycles reaches about 5.6×10^4 , as shown in Fig. 9(b).

Figure 10 shows the change in the frequency response curve of the specimen with input voltage amplitudes of $\Delta V_{in}/2 = 0.36$ V, 0.60 V, 0.90 V, and 1.60 V after 10^7 cycles. Though the peak (f_0) does not change at $\Delta V_{in}/2 \leq 0.90$ V (149.35 kHz - 149.38 kHz), it shifts to 149.27 kHz at $\Delta V_{in}/2 = 1.60$ V after $\Delta\delta_1/2$ rapidly decreases. This result indicates that the rapid decrease is due to the change in f_0 .



(a)



(b)

Fig. 9 (a) Relationship between the net displacement amplitude of the cantilever and number of cycles in the fatigue experiment.

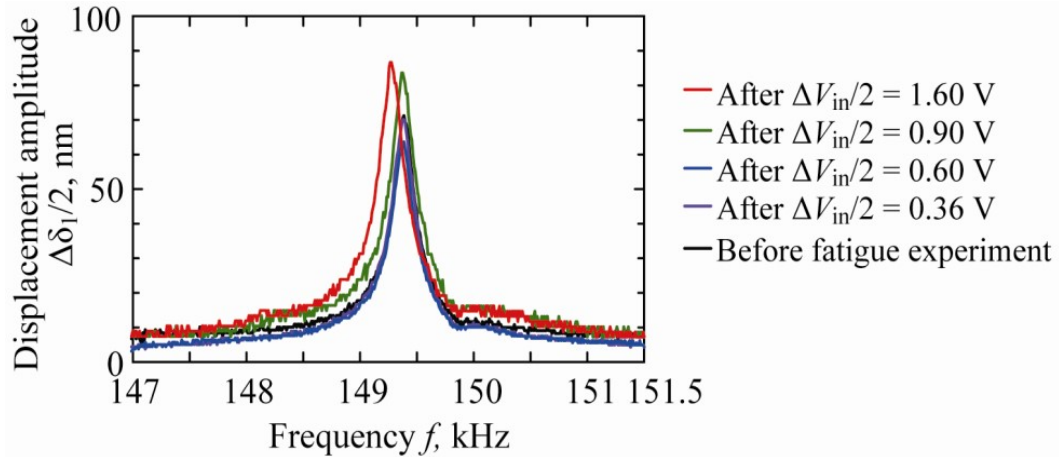


Fig. 10 Change in frequency response curves during the experiment.

4.3 Slip bands

Figure 11 shows FE-SEM images of the upper Cu surface (a) before and (b) after the fatigue test. While no defects exist before the experiment (Fig. 11 (a)), distinct traces appear on the Cu surface in Grain 3 upon the cyclic loading (the white arrow in Fig. 11 (b)) as shown in Fig. 4.

Figure 11(c) shows magnified SEM images of Grain 3. The observed traces have a straight line-like appearance and are inclined at an angle of about 30 degrees to the normal stress applied (x -axis). The stereographic projection of Grain 3 suggests that the traces are slip bands generated by the activity of the slip plane B. The slip bands are composed of concavity and convexity with a width of about 30 nm. Figure 11 (d) shows an SEM image of the upper Cu surface taken from a tilted angle of 70 degrees. The extrusion grows in the upper-right direction, which corresponds to the slip direction 4 in Grain 3, and has a height

of about 40 nm. Although it is very similar to the extrusion/intrusion observed in fatigue of the bulk material, the width (about 30 nm) greatly differs from that of the bulk (about 1 μm).

A crack with a length of about 140 nm is observed along the Cu/Ti interface, as shown in Fig. 11(c). It seems to be initiated at the collision point of extrusion with the Cu/Ti interface where the stress concentrates.

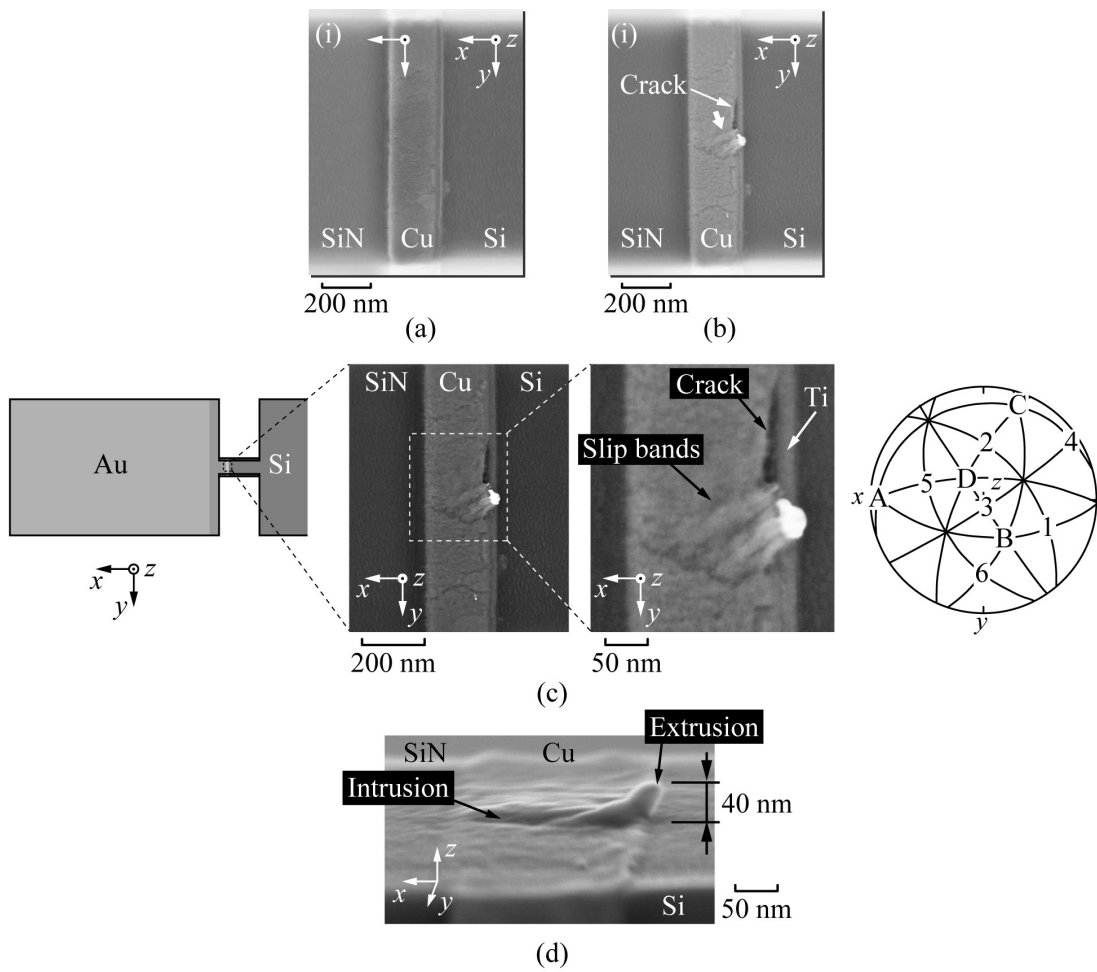


Fig. 11 FE-SEM images of the test section (a) before and (b) after the fatigue experiment, (c) magnified view of Grain 3, and (d) SEM image of the upper surface tilted at 70 degrees.

4.4 Local Stress at Slip Bands

Figure 12(a) shows the Schmid factors (S.F.s) of the primary slip system (B4) in 13 grains on the upper Cu surface. The S.F. of Grain 3 is 0.30, which is smaller than that of Grains 1, 2, 6, 10, 11 and 13. Grains 1 and 13 possess the largest S.F. of 0.31 in the polycrystal.

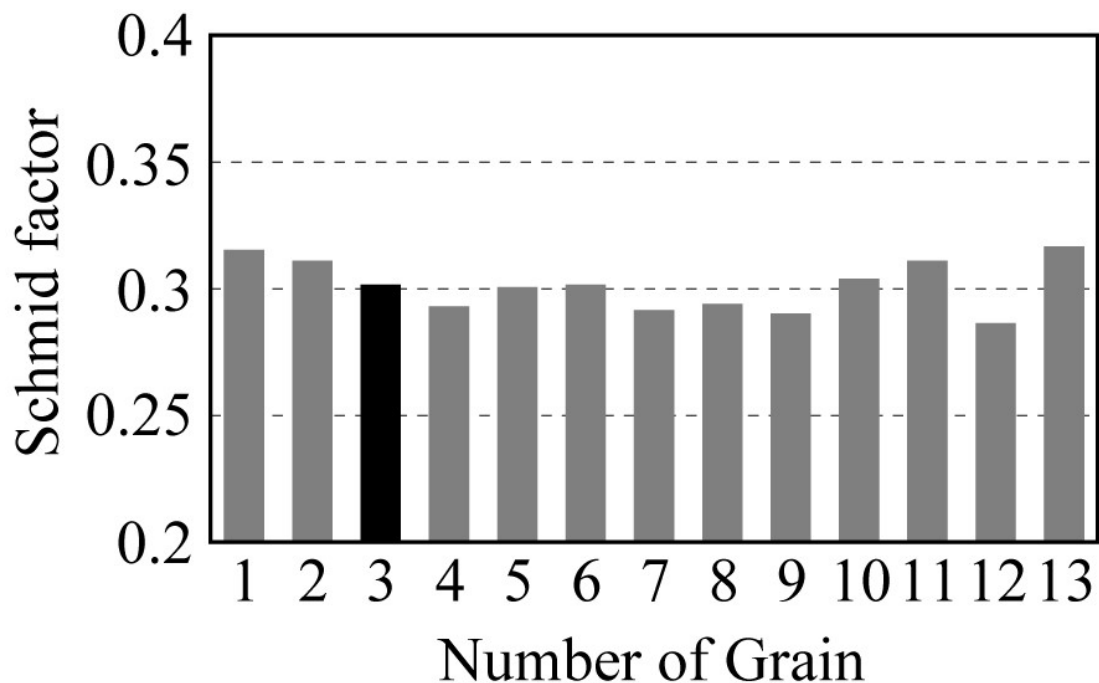
The neighboring grains and surrounding dissimilar materials (Si substrate, Ti layer and SiN layer) result in a stress distribution on each grain owing to the deformation constraint. The microscopic stress conditions in the specimen are identified by elastic FEM. Since there are immeasurable domains (black domains in Fig. 4) around grain boundaries in the EBSD map of the Cu portion, grain boundaries are assumed to exist at the center in the black domains between grains as shown in the illustration in Fig. 12(b). We conduct further FEM analysis for the nano-polycrystalline Cu where we reproduce the exact shapes and crystal orientations of the grains in the specimen model on the surface. We use finer meshes in order to evaluate the precise local stress. On the other hand, since it is impossible to identify the shape and crystal orientation of the grain inside a specimen by EBSD, we construct a model assuming columnar grains on the upper surface where the maximum stress is applied. As the average grain diameter is 190 nm, the columnar grains are 190 nm in height from the upper surface where the highest stress is applied to the bending specimen and Cu is homogeneous below them. Taking into account the crystalline orientations of the columnar grains, the elastic constants of each grain are determined on the basis of the elastic constants in a single crystal ($C_{11(\text{Cu})} = 168.0$ GPa, $C_{12(\text{Cu})} = 75.4$ GPa, $C_{44(\text{Cu})} = 121.0$ GPa).

Figure 12 (b) shows the maximum resolved shear stress, τ_{mrss} , and the slip

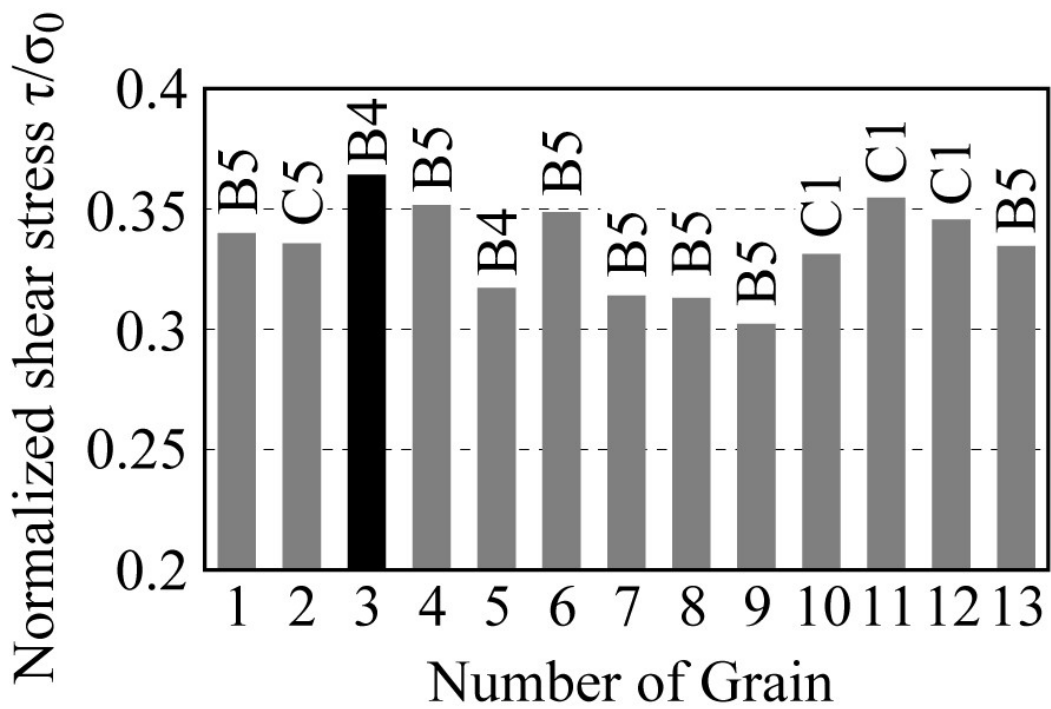
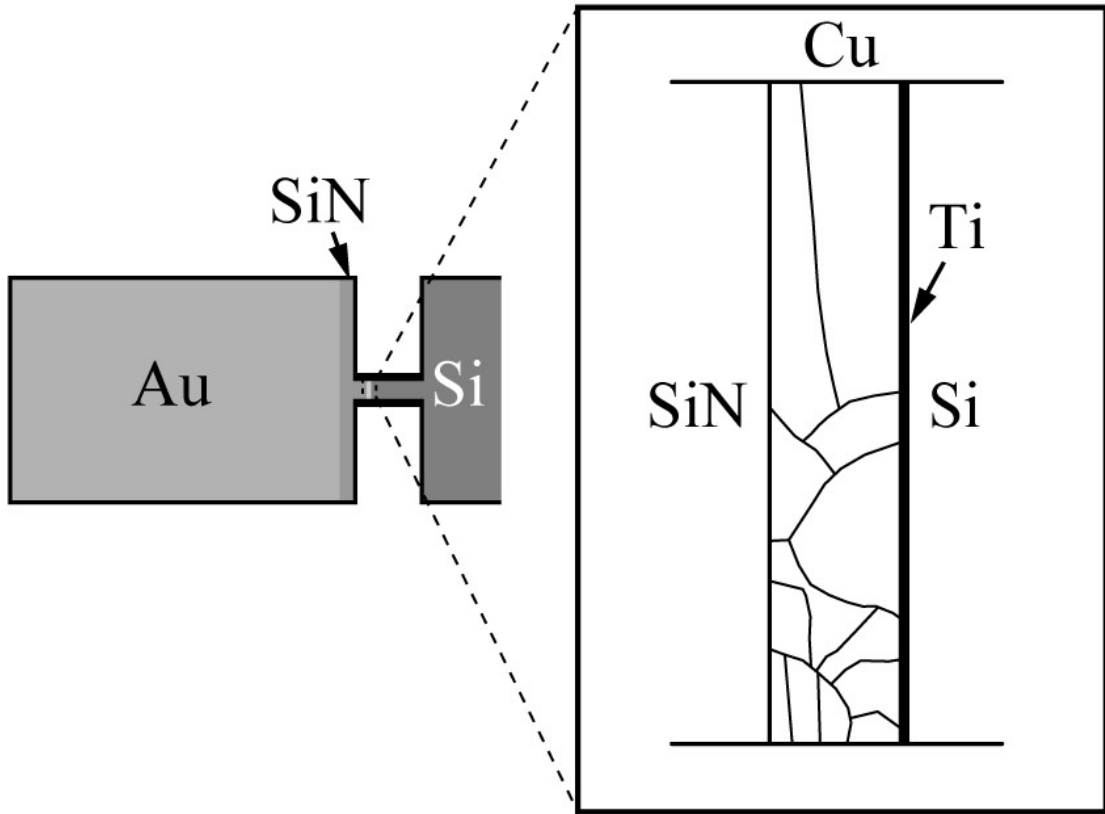
system in each grain. In the figure, τ_{mrss} is normalized by a reference stress σ_0 , which is the x -direction normal stress of an element at the center of the Cu portion on the upper surface. In the 13 grains, Grain 3 possesses the highest τ_{mrss} and the slip system is B4, which corresponds to the slip bands experimentally obtained. This means that the maximum resolved shear stress in the specimen brings about the damage in the high-cycle fatigue testing. In short, the generation of extrusion/intrusion with a width of 30 nm is governed by the nanoscopic stress field due to the deformation constraint. The stress, which is defined on the basis of continuum mechanics, is available as the governing quantity for slip band formation in fatigue of nanoscale materials with an understructure. Taking into account the displacement amplitude for the generation of slip bands ($\Delta\delta/2 = 1224$ nm), the critical resolved shear stress amplitude $\Delta\tau_{\text{crss}}/2$ to generate slip bands is evaluated to be 418 MPa, which is remarkably higher than the $\Delta\tau_{\text{crss}}/2$ of the persistent slip bands formation in the bulk single crystal Cu (≈ 27 MPa).

In the fatigue of Cu bulk material, extrusion/intrusion with a width of about 1 micrometer is formed on the surface. However, they cannot form on the Cu portion in the specimen used here because of the space (200 nm thickness). Moreover, the typical understructure (size $> 1\mu\text{m}$), e.g., vein and ladder structures, which brings about the extrusion/intrusion in fatigue of bulk metal, cannot be formed in this nano-Cu. The new discovery of 30 nm width extrusion/intrusion formation points out that a different mechanism from that in the bulk counterpart brings about the fatigue damage in the nano-material. Though it is governed by the nano-scale crystallographic slip, the detail remains for future works.

The yield stress under monotonic tension of the Cu portion, of which average grain size is 190 nm, was evaluated to be $\Delta\tau_{\text{crss}} = 272$ MPa. This is much larger than that of the single crystalline bulk ($\Delta\tau_{\text{crss}} = 0.5\text{-}1.0$ MPa). In a small component, it is well known that the yield stress increases with decreasing the grain size owing to the influence of grain boundaries (Hall-Petch relation). Moreover, the plastic deformation in the Cu portion is strongly inhibited by surrounding hard dissimilar materials (Si substrate and SiN layer). The high formation stress of 30 nm width extrusion/intrusion might also be due to the influence of nanoscale grain size and the dissimilar materials. Stress concentration near grain boundaries in polycrystalline metal resulted from the deformation constraint among grains would allow for the formation of 30 nm width extrusion/intrusion. It might be a clue for the fatigue mechanism in the future works.



(a)



(b)

Fig. 12 (a) Schmid factor of the primary slip system B4 and (b) normalized maximum resolved shear stress in 12 slip systems in each grain.

Chapter 5 Conclusions

A new test methodology based on resonance vibration of micro/nano structures has been developed to investigate mechanical properties of micro/nano-scale materials. The experimental system consists of a laminated piezoelectric actuator, an operational amplifier, a function generator, a laser Doppler vibrometer and a control computer. The micro/nano-scale specimens are mounted on the piezoelectric actuator with adhesive. The displacement amplitudes of specimens are measured using the laser Doppler vibrometer. As compared to previous methods for small materials, this methodology presents several advantages. The deformation of specimens can be controlled by the resonance modes of specimens, which can be prefabricated by the structural design based on FEM simulation. The sub - strata for supporting specimen and special actuator for applying force are not necessary, then the misalignment between the specimen and the set-up is not an important issue and the fully-reversed cyclic loading at nano-scale is easy to be achieved. Moreover, the deformation of the specimens can be amplified by resonance vibration, and thus easy to measure. Utilizing this vibration-based methodology, three experimental studies on the mechanics of the elastic and fatigue behaviors in the micron and submicron-components are implemented. In the experiments, the anisotropic elastic properties of chiral sculptured thin films at micro-scale is evaluated, the fatigue damage in sub-micrometer single crystal gold is related to changes in internal length scales, and the slip bands in nano-polycrystalline copper under high-cycle fatigue is readily observed.

A STF is a unidirectional and anisotropic module which can be used in vibration, wave and acoustics micro-devices. To evaluate the anisotropic elastic

properties of STF at micro-scale, the newly developed methodology provides a frequency sweep vertical and lateral vibration and monitor displacement of micro-specimen over a frequency range at MHz. Two micro-specimens with design of $30 \times 30 \mu\text{m}^2$ and $15 \times 15 \mu\text{m}^2$, on the top of which added mass are fixed to decrease the resonance frequency to MHz order, are fabricated. Based on the swept-frequency spectra obtained by the testing and numerical analysis, the anisotropic elastic properties of STF are identified. The processing to determine the elastic properties of STFs illustrate that the micro-structural features are important to the dynamic behavior of STFs, and the anisotropic elastic properties of STFs is an interesting feature for further filters, sensors, and waveguides design at micro-scale.

Resonance Vibration fatigue experiments were conducted on single crystal gold cantilevers with different sized sections fabricated by the FIB process. Extrusions/intrusions were formed on the cantilever surfaces in all specimens. The details of extrusion/intrusion indicate a strong specimen size effect. The total width of extrusions/intrusions decreased with the size of the specimen, with variation from hundreds to tens of nanometers, although the width was independent of specimen sizes over $1 \mu\text{m}$. The resolved shear stress to form extrusion/intrusion is much higher than that in bulk gold and is strongly dependent on the specimen size. One suggested interpretation of the results is that the dislocations leave the small crystals before they have a chance to multiply, which leads to dislocation starvation. The emergence of a spatially ordered system (stack) of slip lines during fatigue of the crystal suggests a cooperative nature in the development of extrusion/intrusion in the direction

transverse to the principal slip plane of dislocations.

Resonance fatigue experiment was carried out using a cantilever micro-specimen, in which the test section consists of the Si substrate, and Cu, Ti and SiN nano-layers. The fatigue of fully-reversed loading, which was necessary for the observation of PSB forming, was successfully carried out for the nano-Cu by the developed method. Slip bands with a width of about 30 nm, which were different from the fatigue damage in a Cu bulk counterpart (over 1 μ m), were observed on the surface of Grain 3 along the primary slip system B4 in the Cu portion. Extrusions of about 40 nm height and intrusions were formed in the slip bands. Although their morphology were similar to that in the bulk, the new finding of significantly smaller size in the present material suggests the existence of different damage mechanism. Detailed stress analysis by FEM, taking into account the deformation constraint among grains and between dissimilar materials, indicated that ultra-fine slip bands was governed by the nano-scale shear stress field. The critical resolved shear stress to generate slip bands was evaluated to be $\Delta\tau_{\text{crss}/2} = 418$ MPa, which was remarkably higher than that in the Cu bulk single crystal (≈ 27 MPa). A crack was observed along the Cu/Ti interface. This could have been initiated by the stress concentration induced due to the collision of the extrusion with the Cu/Ti interface.

Reference

- [1] Osterberg P M, Senturia S D. M-TEST: a test chip for MEMS material property measurement using electrostatically actuated test structures. *Microelectromech Systems*, 1997, 6 (2): 107-118.
- [2] Ho C M, Tai Y C. Micro-electro-mechanical systems (MEMS) and fluid flows. *Annual Review of Fluid Mechanics*, 1998, 30: 579-612.
- [3] Yi T C, Kim C J. Measurement of mechanical properties for MEMS materials. *measurement science & technology*, 1999, 10: 706-716.
- [4] Zhao Y P, Yu T X. Failure modes of MEMS and microscale adhesive contact theory. *International Journal of Nonlinear Sciences and Numerical Simulation*, 2000, 1: 361-371.
- [5] Knauss W G, Chasiotis I, Huang Y. Mechanical measurements at the micro and nanometer scales. *Mechanics of Materials*, 2003, 35 (6): 217-231.
- [6] Steven F N, Carol L. An electric induction micro-motor. *Journal of microelectromechanical systems*, 2005, 14 (5): 1127-1143.
- [7] Dai F Y, Zhang W P, Chen W Y, Liu K, Ma G Y, Xiao Q J, Zhang Z R. Survey on MEMS micromotor. *Journal of Micromotors*, 2009, 8 (18): 61-68.
- [8] Zhu Y, Ke C, Espinosa H D. Experimental techniques for the mechanical characterization of one-dimensional nanostructures. *Experimental Mechanics*, 2007, 47 (1): 7-24.
- [9] Zhang T H, Yang Y M, Zhao Y P, Bai Y L. Measurement of mechanical properties of MEMS materials. *Advances in Mechanics*, 2002, 32 (4): 545-562.
- [10] Fu M, Wang H C, Hong Y S. Measurement of mechanical properties of

- materials with micro/nano-meter scale. *Advances in Mechanics*, 2000, 30 (3): 391-399.
- [11] Mazza E, Abel S, Dual J. Experimental determination of mechanical properties of Ni and Ni-Fe microbars. *Microsystem Technologies*, 1996, 2: 197-202.
- [12] Mazza E, Danuser G, Dual H. Light optical deformation measurements in microbars with nanometer resolution. *Microsystem Technologies*, 1996, 2 (2): 83-91.
- [13] Johansson S, Schweitz J Å, Tenerz L, Tiren J. Fracture testing of silicon microelements in situ in a scanning electron microscope. *Journal of Applied Physics* 1988, 63: 4799–803
- [14] Weihs T P, Hong J C, Bravman, Nix W D. Mechanical deflection of cantilever microbeams: A new technique for testing the mechanical properties of thin films. *Journal of Materials Research*, 1988, 3 (5): 931-942.
- [15] Wilson C J, Beck P A. Fracture testing of bulk silicon microcantilever beam subjected to a side load. *Journal of Microelectromechanic System*, 1996, 5: 142–50
- [16] Hirakata H, Takahashi Y, Truong D V, Kitamura T. Role of plasticity on interface crack initiation at free edge and its propagation in nanostructures. *International Journal of Fracture*, 2007, 145: 261-271.
- [17] Sumigawa T, Shishido T, Murakami T, Kitamura T. Interface crack initiation due to nanoscale stress concentration. *Material Science and Engineering A*, 2010a, 527 (18-19): 4796-4803.
- [18] Sumigawa T, Shishido T, Murakami T, Iwasaki T, Kitamura T. Evaluation on

- plastic deformation property of copper nano-film by nano-scale cantilever specimen. *Thin Solid Films*, 2010b, 518: 6040-6047.
- [19] Sumigawa T, Murakami T, Kitamura T. Fatigue strength of the Cu/Si interface in nano-components. *Material Science and Engineering A*, 2011, 528: 5158-5163.
- [20] Zhang T H, Yang Y M, Zhao Y B, Yu T X, Sun Q P. Research on tension measurements for minsize materials. *Journal of Mechanical strength*, 2001, 23 (4): 430-436.
- [21] suchiya T, Inoue A, Sakata J, Hashimoto M, Yokoyama A and Sugitomo M. Fatigue test of single crystal silicon resonator. *Technical Digest 16th Sensor Symp.*, Kawasaki, June 1998 pp 277–80.
- [22] Friswell M I, Mottershead J E. *Finite Element Model Updating in Structural Dynamics*, Kluwer Academic Publishers, Dordrecht, 1995.
- [23] Michael D U, Dennis M D, Jeffrey N F, William D N. Sample dimensions influence strength and crystal plasticity. *Science*, 2004, 305 (8): 986-989.
- [24] Sylwestrowicz W, Hall E O. The deformation and ageing of mild steel. *Proceedings of the Physical Society, part B*, 1951, 64: 747.
- [25] Petch, N J. The cleavage strength of polycrystals. *Journal Iron Steel Institute*, 1953, 174: 25-28.
- [26] Yip S. Nanocrystals: The strongest size, *Nature*, 1998, 391: 532-533.
- [27] Xu J, Zhang G P. Effects of grain size and initial immobile dislocation density on fatigue behavior of polycrystalline metals. *Material Science & Engineering A*, 2014, 590: 194-198.
- [28] Shang F L, Kitamura T, Sumigawa T. Experimental study on interface

- strength of micro/nano-materials and their structures. *Advances in Mechanics*, 2008, 38 (4): 437.
- [29] Nakamura N, Ogi H, Hirao M. Elastic constants of chemical-vapor-deposition diamond thin films: resonance ultrasound spectroscopy with laser-Doppler interferometry. *Acta Materialia*, 2004, 52, 765-771.
- [30] Robbie K, Brett M J, Lakhtakia A. First thin film realization of a helicoidal bianisotropic medium. *Journal of Vacuum Science and Technology A*, 1995, 13 (6): 2991-2993.
- [31] Robbie K, Brett M J. Sculptured thin films and glancing angle deposition: growth mechanics and applications. *Journal of Vacuum Science and Technology A*, 1997, 15 (3): 1460–1465.
- [32] Hirakata H, Matsumoto S, Takemura M, Suzuki M, Kitamura T. Anisotropic deformation of thin films comprised of helical nanosprings. *International Journal of Solids and Structures*, 2007, 44: 4030-4038.
- [33] Ogi H, Shimoike G, Hirao M, Takashima K, Higo Y. Anisotropic elastic-stiffness coefficients of an amorphous Ni-P film. *Journal of applied physics*, 2002, 91 (8): 4857.
- [34] McPherson R. The relationship between the mechanism of formation, microstructure and properties of plasma-sprayed coatings. *Thin solid films*, 1981, 83 (3): 297-310.
- [35] Liu Y, Nakamura T, Srinivasan V, Vaidya A, Gouldstone A, Sampath S. Non-linear elastic properties of plasma-sprayed zirconia coatings and associated relationships with processing conditions. *Acta Materialia*, 2007,

- 55 (14): 4667-4678.
- [36] Leigh S H, Lin C K, Berndt C C. Elastic response of thermal spray deposits under indentation tests. *Journal of American Ceramic Society*, 2005, 80 (8): 2093-2099.
- [37] Djemia P, Dugautier C, Chauveau T, Dogheche E, De Barros MI, Vandembulcke L. Mechanical properties of diamond films: A comparative study of polycrystalline and smooth fine-grained diamonds by Brillouin light scattering technique. *Journal of Applied Physics*, 2001, 90: 3771.
- [38] Moretti AL, Robertson WM, Fisher B, Bray R. Surface-enhanced Brillouin scattering on silver films. *Physics Review B*, 1985, 31: 3361.
- [39] Tan Y, Shyam A, Choi W, Lara-Curzio E, Sampath S. Anisotropic elastic properties of thermal spray coatings determined via resonant ultrasound spectroscopy. *Acta Materialia*, 2010, 58: 5305-5315.
- [40] Limarga A M, Duong T L, Gregori G, Clarke D R. High-temperature vibration damping of thermal barrier coating materials. *Surface Coating Technology*, 2007, 202: 693.
- [41] Cook L S, Wolfenden A, Brindley W J. Temperature dependence of dynamic Young's modulus and internal friction in LPPS NiCrAlY. *Journal of Material Science*, 1994, 29: 5104-5108.
- [42] Gregori G, Li L, Nychka J A, Clarke D R. Vibration damping of super alloys and thermal barrier coatings at high-temperatures. *Material Science & Engineering A*, 2007, 466: 256.
- [43] Nakamura N, Ogi H, Hirao M. Elastic constants of chemical-vapor-deposition diamond thin films: resonance ultrasound

- spectroscopy with laser-Doppler interferometry. *Acta Materialia*, 2004, 52, 765-771.
- [44]Ma B T, Laird C. Overview of fatigue behavior in copper single crystals—II. Population, size distribution and growth kinetics of Stage I cracks for tests at constant strain amplitude *Acta Metallurgica*, 1989, 37(2): 337-348.
- [45]Mugrabi H. Dislocation wall and cell structures and long-range internal stresses in deformed metal crystals. *Acta Metallurgica*, 1983, 31(9): 1367-1379.
- [46]Suresh S. *Fatigue of material* (2nd ed.), Cambridge University Press, Cambridge, UK; 1998.
- [47]Zhang G P, Schwaiger R, Voljert C A, Kraft O. Effect of film thickness and grain size on fatigue-induced dislocation structures in Cu thin films. *PHILOSOPHICAL MAGAZINE LETTERS*, 2003, 83 (8): 477-483.
- [48]Read D T. Tension-tension fatigue of copper thin films. *International Journal of Fatigue*, 1998, 20 (3): 203-209.
- [49]Schwaiger R, Kraft O. High cycle fatigue of thin silver films investigated by dynamic microbeam deflection. *Scripta Materialia*, 1999, 41 (8): 823-829.
- [50]Schwaiger R, Dehm G, Kraft O. Cyclic deformation of polycrystalline Cu films. *Philosophical Magazine*, 2003, 83 (6): 693-710.
- [51]Schwaiger R, Kraft O. Size effects in the fatigue behavior of thin Ag films. *Acta Materialia*, 2003, 51 (1): 195-206.
- [52]Kraft O, Schwaiger R, Wellner P. Fatigue in thin films: lifetime and damage formation. *Material Science & Engineering A*, 2001, 319: 919-923.

- [53] Sumigawa T, Murakami T, Shishido T, Kitamura T. Cu/Si interface fracture due to fatigue of copper film in nanometer scale, *Material Science & Engineering A*, 2003, 527: 6518-6523.
- [54] Lakhtakia A. Sculptured thin films: accomplishments and emerging uses. *Materials Science and Engineering C*, 2002a, 19: 427–434.
- [55] Lakhtakia A. Microscopic Model for Elastostatic and Elastodynamic Excitation of Chiral Sculptured Thin Films. *Journal of Composite Materials*, 2002b, 36: 1277.
- [56] Zhang J Y, Zhang X, Liu G, Wang R H, Zhang G J, Sun J. Length scale dependent yield strength and fatigue behavior of nanocrystalline Cu thin films. *Material Science & Engineering A*, 2011, 528: 7774-7780.
- [57] Judelewicz M, Kunzi H U, Merk N, Ilshner B. Microstructural development during fatigue of copper foils 20–100 μm thick. *Material Science & Engineering A*, 1994, 186: 135-142.
- [58] Sumigawa T, Matsumoto K, Fang H, Kitamura T. Formation of slip bands in nano-polycrystalline copper under high-cycle fatigue of Si/Ti/Cu/SiN nano-scale material. *Material Science & Engineering A*, 2014, 608: 221-228.

List of published papers

- [1] Fang H, Sumigawa T, Shiohara R, Kitamura T, Size dependence of fatigue damage in sub-micrometer single crystal gold. *Materials Science & Engineering A*, 2014, 618: 416–423.
- [2] Fang H, Sumigawa T, Mastumoto K, Kitamura T. Anisotropic elastic properties of chiral sculptured thin films at micro-scale evaluated by resonance frequency spectra. *European Journal of Mechanics - A/Solids*, 2015, 40: 510-517.
- [3] Fang H, Wang TJ, and Chen X. Model updating of lattice structures: A substructure potential energy (SPE) approach, *Mechanical Systems and Signal Processing*, 2011, 25(5), 1469-1484.
- [4] Fang H, Estimating severity of damage in lattice structures utilizing substructure modal data, *Journal of Vibration and Acoustics-ASME*, 2010, 133(3): 034502-5.
- [5] Sumigawa T, Fang H, Kawai E, Kitamura T. Mechanics of fracture in nanometer-scale components. *Mechanical Engineering Reviews*, 2014, 1: 1 – 20.
- [6] Fang H. Damage localization and severity estimate for lattice material, *Advanced Materials Research*, 2010, 146-147, 789-792.
- [7] 方辉, 基于子结构能量的点阵结构损伤诊断方法研究, *振动与冲击*, 2010, 30 (8): 12-18.
- [8] 方辉, 澄川贵志, 北村隆行, 基于振动的亚微米阵列薄膜弹性参数辨识, *中国科学: 物理学、力学、天文学*, 2014, 44, 1196-1202.
- [9] 冯晓伟, 冯高鹏, 方辉, 不同应变率下冰破坏特性的试验研究, *应用*

力学学报, 2015, 出版中.

- [10] Fang H. Improved damage quantification method based on substructure modal strain energy, Proceeding of RISK ANALYSE 2010.
- [11] Sumigawa T, Matsumoto K, Fang H, Takayuki Kitamura. Formation of Slip Bands in Poly-Crystalline Nano-Copper under High-Cycle Fatigue of Fully-Reversed Loading. *Materials Science & Engineering A*, 2014, 608, 221-228.
- [12] Wang J, Shu WL, Fang H and Kamlah M, Phase field simulation on the poling process and nonlinear behavior of ferroelectric polycrystals with semiconducting grain boundaries, *Smart Materials and Structure*, 2014, 23(9), 095016.
- [13] Li GP, Wang J, Shimada T, Fang H, and Kitamura T, Strain-induced polarity switching of magnetic vortex in $\text{Fe}_{1-x}\text{Ga}_x$ alloys with different compositions, *Journal of Applied Physics*, 2014, 115, 203911.
- [14] Li GP, Wang J, Shimada T, Fang H, and Kitamura T, Control of the polarity of magnetization vortex by torsion, *Applied Physics Letter*, 2013, 103, 242413.